university of groningen / faculty of science and engineering / zernike institute for advanced materials

FACULTY OF SCIENCE AND ENGINEERING

BACHELOR DEGREE IN PHYSICS

Calculations of the Casimir Force for Multi-layer Systems: from Isotropic Materials to Topological Insulators

Supervisor
Prof. George Palasantzas

Author
Elena Zancanaro

Second Supervisor
Prof. Antonija Grubisic-Cabo

Daily Supervisor
Gustavo Chavez Ponce de Leon

ACADEMIC YEAR 2023-2024

Date of Thesis Submission 01/07/2024

To my family

Abstract

The Casimir force arises from boundary-dependent modifications of the zero-point energy due to fluctuations in the electromagnetic field. This force, calculated between two bodies with known optical properties, typically manifests as an attractive interaction. However, theoretical predictions suggest that creating a repulsive Casimir force is possible by modifying boundary conditions. This thesis explores various approaches to achieving a repulsive Casimir force, particularly in using three-dimensional topological insulators, a novel class of materials with unique electronic and optical properties.

The research reveals that variations in the thickness of multilayer systems meaningfully impact the Casimir force, with thinner layers exhibiting more pronounced effects. Introducing surface conductivity alters the topological force contrast (TFC), and larger theta values lead to more substantial changes. Complex interdependencies are observed in systems with multiple layers and varying thicknesses, with certain configurations enhancing the reduction factor of the Casimir force. Simplified toy models effectively predict general trends, although real materials reveal additional complexities that need consideration. These insights guide the design of nanoscale devices by strategically manipulating material properties and layer thicknesses to control the Casimir force.

In only one case, a significant enhancement of the Casimir force was observed as reported in Figure 4.3. However, this was due to geometrical configuration rather than the topological response of the material. Despite numerous theoretical predictions, experimental evidence of repulsive Casimir forces remains elusive. This thesis emphasizes the need for improved modelling of topological insulators to understand both bulk and surface contributions to the Casimir force. Such advancements could inspire experimental efforts to measure repulsive Casimir forces, potentially leading to significant breakthroughs in nanotechnology applications.

Outline

This thesis explores the subtle interplay of the Casimir force in multilayer systems through a systematic analysis of varying parameters.
A two-layer system establishes a baseline for Casimir force calculations. In section 4.1 a third layer with variable thickness, exploring layer-dependent interactions is introduced. In subsection 2.3.3, surface conductivity is introduced, adding a material property dimension to the two-layer system. The same analysis is conducted in a liquid gap as reported in section 3.1. In section 4.2, the analysis is generalized to N layers, varying the thickness of each layer except the first. In section 4.3, dual-sided surface conductivity is incorporated into a three-layer system, presenting a nuanced interaction between surface properties and layer thickness variations. Each step offers unique insights into the Casimir force and reduction factor, laying the groundwork for understanding the impact of layer variations and surface properties. Comparative analyses highlight trends and unexpected behaviours, guiding practical applications in nanoscale device design. This systematic exploration contributes to a comprehensive understanding of Casimir interactions in multilayer structures, with implications for optimizing nanotechnological devices.

Acknowledgment

I would like to express my sincere gratitude to Prof. George Palasantzas for his invaluable guidance, expertise, and support throughout the course of this research and whole bachelor.
I am also thankful to Prof. Antonija Grubisic-Cabo for her contributions to this work.
Special thanks to Gustavo Chavez Ponce de Leon for his continuous support and assistance in navigating the challenges encountered during this research endeavor. His expertise and dedication have been invaluable.
A mamma e papà, il vostro amore, il vostro incoraggiamento e i vostri sacrifici sono stati la forza trainante del mio percorso accademico, grazie per tutto.
Ad Ale, alle nonne e a Zia, il vostro amore incondizionato e il vostro sostegno costante hanno portato gioia e risate in ogni momento di questo viaggio. A tutta la mia famiglia e amici, grazie per il vostro amore, il vostro incoraggiamento e la vostra incondizionata fiducia nelle mie capacità.
To Jordy, thank you for proofreading this thesis and for your support during this period.

Contents

List of Figures

Chapter 1

A Macroscopic Quantum Phenomenon

The development of quantum mechanics has provided a description of reality that often disobeys all classical logic and prediction. One of the most important results, still tied to unresolved issues today, is the existence of vacuum energy. In classical electrodynamics, there is no reason why there should be electromagnetic radiation in a vacuum. However, as early as 1912, while studying the black body spectrum, Planck discovered the concept of zero-point energy, starting from the sole hypothesis that radiation consisted of discrete and indistinguishable energy quanta. From that moment on, in a series of subsequent events, quantum theory took shape, and it was from the quantization of the electromagnetic field that vacuum energy reemerged [1].

According to quantum field theory, the vacuum is not truly empty despite being devoid of matter and radiation. It can be described as a quantized electromagnetic (EM) field consisting of oscillators at all frequencies (ω). Consequently, the energy in the ground state of these harmonic oscillators is not zero but rather $\approx\omega/2$, indicating that the vacuum possesses a non-zero energy density. This forms the foundation of quantum fluctuations [2], and more about this can be found in Appendix A. While the presence of zero energy seems inconsequential, it gives rise to many macroscopic phenomena. For instance, the attraction between two atoms or molecules arises from the instantaneous dipole moment created by the motion of electron clouds, a result of quantum fluctuations. These instantaneous dipole moments generate fluctuating EM fields, inducing similar dipole moments in nearby atoms or molecules. On average, the dipole moment of an atom or molecule is zero. However, in the quantum theory developed by Fritz London in 1930, the dispersion of the dipole moment operator is non-zero, resulting in correlations between the EM field fluctuations generated by both atoms or molecules [3]. This concept of vacuum energy directly connects to the roots of the Casimir effect. The Van der Waals attraction occurs between two nearby atoms or molecules, even nonpolar ones. This type of interaction extends to neutral macroscopic bodies and originates from the motion of the electric charges within them, generating fluctuating electromagnetic fields in the space between the objects. These fields induce transient dipole moments in the molecules, causing their interaction. Therefore, the Van der Waals interaction is purely quantum; London's work confirms and completes this assertion by demonstrating that it is a non-relativistic effect, as

his results depend on Planck's constant h, but not on the speed of light in a vacuum c [4].
A quantum and non-relativistic Van der Waals force manifests in the limit where two atoms, molecules, or macroscopic bodies are close to each other (a few nanometers apart). This distance allows a virtual photon emitted by one atom to reach the other within a time equal to or less than its lifetime, producing instantaneous dipole moments in both atoms; this is referred to as the non-retarded Van der Waals force [5]. If the distance between the atoms increases, the non-retarded Van der Waals force does not exist. However, the dispersion of the electromagnetic field is still non-zero, resulting in the emergence of dipole moments and an attractive force between the atoms. This long-range interaction, known as the Casimir-Polder force, is a relativistic extension of the Van der Waals force and depends on the polarizability of the atoms [3], [6].

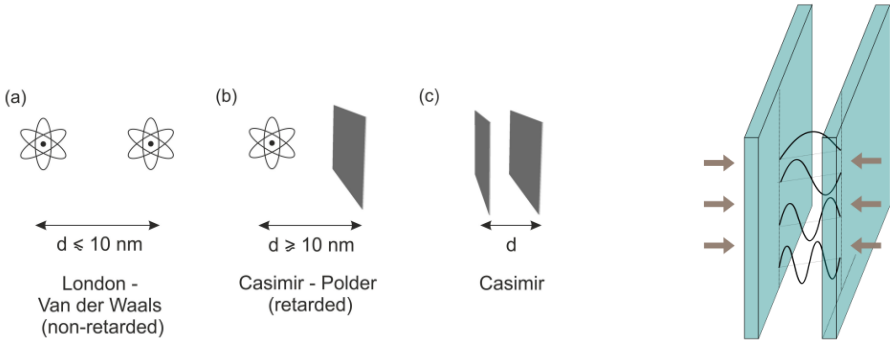

Figure 1.1: (A) Schematics of the different types of dispersion forces: (a) non-retarded London-van der Waals, (b) retarded Casimir-Polder and (c) Casimir interaction. (B) The Casimir effect's principal setup involves quantizing electromagnetic waves confined between two parallel plates. This quantization gives rise to an attractive force between the plates, symbolized by brown arrows.

On a macroscopic scale, Casimir predicted the existence of an attractive force between two parallel, perfectly conducting neutral plates placed in a vacuum. This interaction, known as the Casimir effect, is thus an extension of the Casimir-Polder force within material boundaries. The theoretical demonstration of the existence of the Casimir force is obtained by considering an electromagnetic field inside a parallelepiped with sides $L_x \equiv L_y = L$ and L_z, consisting of two perfectly conducting plates, each with an area L^2, placed at a distance $d \equiv L_z$ as shown in Figure 1.1b [7]. This technique yields the following expression for the Casimir energy [8]:

$$\Delta E = -\frac{\pi^2 \hbar c}{720 d^3} \tag{1.1}$$

This result indicates an attractive force between the perfectly conducting parallel plates due to the vacuum fluctuations of the electromagnetic field. The derivation of this result can be found in Appendix C. The negative sign indicates the attractive nature of the Casimir force. The Casimir effect has been experimentally observed, providing remarkable confirmation of the quantum vacuum fluctuations predicted by quantum field theory.

The Casimir force between the plates can be calculated by taking the derivative of the Casimir energy with respect to the separation distance d [4]:

$$F_{\text{Casimir}} = -\frac{\partial(\Delta E)}{\partial d} = \frac{\pi^2 \hbar c}{240 d^4} \tag{1.2}$$

This expression shows that the Casimir force is inversely proportional to the fourth power of the separation distance between the plates. The force becomes stronger as the plates get closer together, following the theoretical predictions [2].

The Casimir force, though weak, offers a unique window into the connection between the quantum world and our macroscopic reality. Measuring this force, however, is no easy accomplishment [9]. Early experiments, like Sparnay's in 1958, were groundbreaking but faced significant challenges [9]. Achieving the necessary precision in surface separation and minimizing unwanted electrostatic forces proved challenging. Techniques like spring dynamometers and balancing forces with applied potentials were employed, but limitations in accuracy remained [10]. Later advancements, such as Lamoreaux's torsion pendulum and Mohideen's atomic force microscopy, addressed these issues. Torsion pendulums offered more significant control over separation distances, while atomic force microscopy provided exceptional sensitivity in measuring the minute deflections caused by the Casimir force [11].

While not always achieving perfect agreement with theory, these experiments progressively refined our understanding of the Casimir force. Each iteration highlighted the significance of surface cleanliness, material properties, and precise distance control. More about the experiments that led to the discovery of the Casimir effect can be found in Appendix D.

Nowadays, the Casimir effect has transitioned from theoretical curiosity to practical consideration in the latter years, thanks to recent advancements in nanofabrication techniques [12]. This progression enables precise control and tuning of the Casimir force, opening up possibilities for innovative device applications. Within this context, two prominent research approaches have emerged, each offering unique avenues for exploiting the Casimir effect [13].

The first approach leverages geometric modifications to manipulate the Casimir force, adding new nanostructure functionalities. Research like the one by A. W. Rodriguez et al. has shown that employing a new computational approach for Casimir forces in various geometries can yield substantial insights [14]. Their findings highlight nonadditive and nonmonotonic variations in Casimir forces influenced by lateral walls. This innovative method is a valuable tool for comprehending and predicting the behaviour of Casimir forces in intricate micro- and nanostructured systems, which is crucial for developing NEMS/MEMS technologies like resonators. The second approach focuses on the material properties, specifically the response functions of various materials, to modulate the Casimir force. Research by G. Palasantzas et al. has shown that Casimir forces have significant potential applications in micro- and nanosystems. Their paper [15] discusses how these quantum fluctuations can be harnessed for actuation in such systems, emphasizing the critical role

of both van der Waals and Casimir interactions in adhesion processes. The study stresses the importance of carefully selecting material properties and optimizing system designs to effectively manage these forces, thereby enhancing the performance and stability of nanoscale devices. This thesis aims to bridge the gap between these two approaches by exploring the combined effects of geometric structuring and the unique properties of topological insulators. By integrating multilayer geometries with the distinctive characteristics of topological insulators (TIs), this research seeks to advance the understanding and practical utilization of the Casimir effect in nanoscale devices. The potential to harness and control the Casimir force through this combined approach could pave the way for novel applications in NEMS/MEMS and beyond, contributing significantly to the field of nanotechnology.

1.1 Proximity Force Approximation

The Proximity Force Approximation (PFA) is a valuable computational tool that simplifies the calculation of forces by discretizing the interaction surface into infinitesimal plates. This method systematically summates forces between these small, parallel segments, typically used in plane-plane geometry (pp). In the sphere-plate geometry (sp), when the separation distance between the sphere and the plate is much smaller than the radius of the sphere, the curved surface of the sphere is approximated as a series of infinitesimally small, parallel plates.

$$F_{\mathrm{sp}} \approx \sum_{i,j} f_{\mathrm{pp}}\left(z\left(x_i, y_j\right)\right) \Delta x_i \Delta y_j \tag{1.3}$$

As the discretization approaches an infinitesimal scale, the summation transforms into a double-integral

$$F_{\mathrm{sp}} \approx \iint_{\mathcal{S}^2} f_{\mathrm{pp}}(z(x,y)) dx dy \tag{1.4}$$

For large radii ($R \gg d$), the force equation further simplifies to

$$F_{\mathrm{sp}} \approx 2\pi R \int_d^\infty f_{\mathrm{pp}}(z) dz \tag{1.5}$$

The total force exerted is contingent upon the radius of the sphere, expressed as

$$F_{\mathrm{sp}} \approx 2\pi R E_C(d) \tag{1.6}$$

Here, $E_C(d)$ is the energy. The theoretical upper limit of this force is defined by

$$F_{\text{Ideal}}\left(d\right) = \frac{\pi^3 \hbar c R}{360 d^3} \tag{1.7}$$

An intrinsic reduction factor (η) is defined as exclusively reliant on material properties and independent of the sphere's radius

$$\eta = \frac{F_{\text{sp}}(d)}{F_{\text{Ideal}}(d)} \tag{1.8}$$

1.1.1 Limitations of the Model

While the Proximity Force Approximation (PFA) is a powerful method for estimating interactions, it has several limitations. First, the PFA assumes that the interacting bodies can be approximated as a series of infinitesimally small, parallel plates, which works best for nearly parallel surfaces and does not accurately account for more complex or curved geometries [16]. Additionally, the accuracy of the PFA diminishes as the separation distance between the interacting surfaces decreases. At very short distances, the discrete nature of matter and surface roughness can significantly affect the interaction forces, which the PFA does not account for. The PFA also assumes material homogeneity, ignoring variations in material properties at the nanoscale, such as inhomogeneities or surface coatings [17].

Despite its limitations, the Proximity Force Approximation (PFA) remains a highly useful tool in nanoscale physics and engineering. Its primary advantage lies in its computational simplicity, allowing for estimating forces between bodies with relatively straightforward mathematical calculations. The PFA is particularly effective for systems with nearly parallel surfaces and small separations, and it is common in many practical applications, such as microelectromechanical systems (MEMS) and nanotechnology. The PFA enables researchers and engineers to predict interaction forces quickly and efficiently by converting complex geometries into simpler, parallel plate approximations. Additionally, the PFA provides valuable insights into the behaviour of quantum and electromagnetic forces at small scales, contributing to the design and optimization of nanoscale devices. Its ability to handle a variety of materials and conditions, albeit under idealized assumptions, makes it a widely adopted method in the study of intermolecular and surface forces.

1.2 Casimir Effect in the Presence of Semi-Infinite Surfaces

We first determine the electromagnetic fluctuations to calculate the Casimir force in the presence of semi-infinite surfaces. These fluctuations allow us to integrate the average value of Maxwell's stress tensor normal to the surface, thereby obtaining the Casimir force. For detailed information on electromagnetic fields and the Maxwell equations that lead to the stress tensor, please refer to Appendix E. The general problem of calculating Casimir Energy for infinite plates involves analytic functions in the complex plane, as detailed in Appendix C. However, a simpler solution is possible when the geometry consists of two semi-infinite planes separated by a gap, as illustrated in Figure 1.2a. Lifshitz first examined this specific configuration in 1954 [10]. In the preceding discussion, we assumed an infinite dielectric permeability of the media as described in Equation 1.2.

However, dielectric permeability is frequency-dependent and denoted as $\varepsilon(\omega)$, accounting for different media and their frequency-dependent properties. Lifshitz's discoveries lay the groundwork for broadening the scope to encompass configurations with multiple surfaces and diverse materials. [2]. In this framework, the reflection coefficients play the main role.

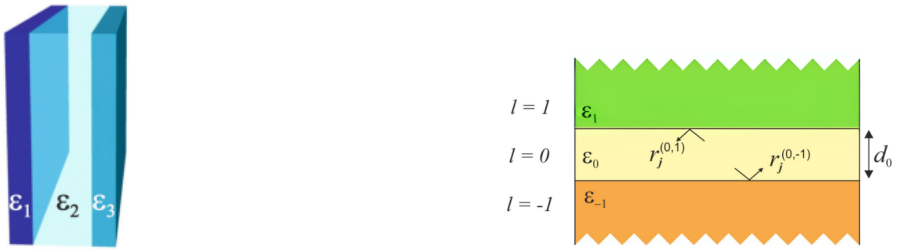

(a) (b)

Figure 1.2: (A) Scheme of a plane-parallel system with a gap (that might be different from the vacuum) [10]. (B) Diagram illustrating the interaction between two semi-infinite materials ($l = 1$ and $l = -1$) through the Casimir-Lifshitz force, mediated by material $l = 0$. Each material l is characterized by its dielectric function ε_l. The Fresnel coefficient at the interface between materials l and l' is indicated as $r_j^{(l,l')}$.

1.3 Casimir force for multi-layers systems

The Casimir force between a sphere with radius R and a flat plate, separated by a distance gap, can be calculated using a sphere-plate geometry (sp) configuration. Assuming the material is isotropic and applying the proximity force approximation (PFA), the Casimir force is given by:

$$F_{sp} = 2\pi R\mathcal{F} \tag{1.9}$$

where $\mathcal{F}$ is the plate-plate free energy per unit area given by

$$\mathcal{F} = \sum_{n=-\infty}^{\infty} \mathcal{F}_n \tag{1.10}$$

where

$$\mathcal{F}_n = \frac{k_B T}{2} \int \frac{dk_\parallel^2}{(2\pi)^2} \ln\left(\det\left[\mathbb{I} - \mathbb{R}_1\mathbb{R}_2 e^{-2k_\perp d}\right]\right) \tag{1.11}$$

where

$$k_\perp = \sqrt{k_\parallel^2 + \epsilon_g\mu_g\left(\frac{\hbar\xi_n}{\hbar c}\right)^2} \tag{1.12}$$

where the reflection matrices $\mathbb{R} = \mathbb{R}\left(|\xi_n|, k_\parallel\right)$must be analytically continued to the n-th Matsubara frequency ($\hbar\xi_n = 2\pi k_B T n$). Here, $\epsilon_g = \epsilon_g\left(i\,|\xi_n|\right)$ $\left(\mu_g = \mu_g\left(i\,|\xi_n|\right)\right)$ represents the permittivity, permeability, of the gap [18].

As electromagnetic waves can be polarized in different ways when discussing reflection and trans-

mission at interfaces, two common polarizations are considered:

- **s-Polarization (TE - Transverse Electric)**: The electric field is perpendicular to the plane of incidence.
- **p-Polarization (TM - Transverse Magnetic)**: The magnetic field is perpendicular to the plane of incidence.

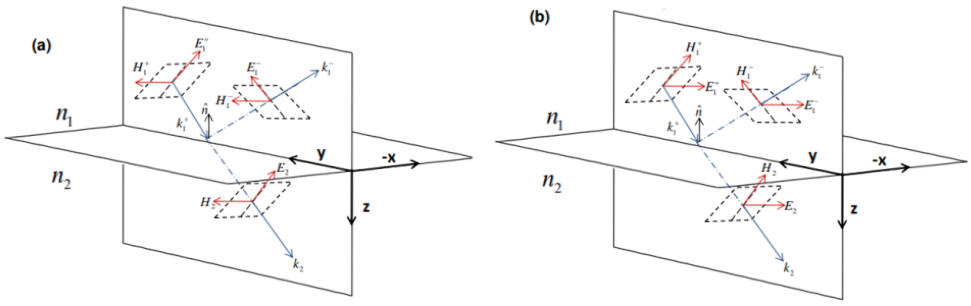

Figure 1.3: Geometries of incident plane waves with (a) p polarization (or TM) and (b) s polarization (or TE).

Reflection coefficients describe how much of an incident wave is reflected by a surface. These coefficients depend on the polarization of the wave:

- r_{ss}: Reflection coefficient for s-polarized waves.
- r_{pp}: Reflection coefficient for p-polarized waves.
- r_{sp}: Cross-polarization reflection coefficient from s to p polarization.
- r_{ps}: Cross-polarization reflection coefficient from p to s polarization.

It follows that the reflection matrix at an imaginary frequency can be written as:

$$\mathbb{R} = \begin{bmatrix} r_{ss}\left(i\xi_n, k_\parallel\right) & r_{sp}\left(i\xi_n, k_\parallel\right) \\ r_{ps}\left(i\xi_n, k_\parallel\right) & r_{pp}\left(i\xi_n, k_\parallel\right) \end{bmatrix} \tag{1.13}$$

Under the assumption that all materials present in-plane symmetry, we can simplify the contribution of the n-th Mastubara frequency as follows

$$\mathcal{F}_n = \frac{k_B T}{2} \frac{1}{8\pi d^2} \int_{x_n}^{\infty} x \ln\left(\det\left[\mathbb{I} - \mathbb{R}_1 \mathbb{R}_2 e^{-x}\right]\right) dx \tag{1.14}$$

where $x = 2k_\perp d$ and $x_n = \frac{\hbar \xi_n}{\left(\frac{\hbar c}{2d\sqrt{\epsilon_g \mu_g}}\right)}$ [18].

To numerically implement these equations, we will introduce a cutoff for the Matsubara frequencies

and for the x integral. In addition, we will evaluate the integral using the trapezoid method with a mesh defined by the spacing Δx. Mathematically, our approximation is given by

$$F_{sp} \approx (2\pi R)\left(\frac{k_B T}{8\pi d^2}\right) \sum_{n=0'}^{n_{\text{cutoff}}} \sum_{m=x_n}^{x_{\max}} \frac{I_n(x_{m-1}) - I_n(x_m)}{2} \Delta x \tag{1.15}$$

where

$$I_n(x) = x \ln\left(\det[\mathbb{I}] - \mathbb{R}_1 \mathbb{R}_2 e^{-x}\right) \tag{1.16}$$

$$\mathbb{R} = \mathbb{R}\left(k_\perp = \frac{x}{2d}, i\xi_n\right) \tag{1.17}$$

here, the apostrophe means that term $n = 0$ must be multiplied by a factor of $1/2$ [19]. In this thesis, we will explicitly solve for the reflection matrix at imaginary frequencies using the transfer matrix formalism that will depend on the perpendicular component of the wave-vector in the gap $(k_\perp)$, and the imaginary frequency ξ as will be seen in section 2.2.

A more comprehensive approach for calculating the Casimir energy considers the effects of non-ideal mirrors that scatter light in various directions, a phenomenon known as non-specular reflection. Non-specular reflection accounts for the imperfections and roughness of real surfaces, where the reflected light is diffused rather than being reflected in a single, predictable direction as in specular reflection. This results in a more accurate depiction of the physical reality, as perfect specular reflection is an idealization that rarely occurs in practical situations. Non-specular reflection can significantly impact the Casimir force calculations, especially at shorter distances and with materials that have complex surface properties.

Details on this generalized approach, including the mathematical formulations and numerical methods used to account for non-specular reflections, can be found in Appendix G. This appendix provides a deeper insight into how non-ideal surface interactions are modeled and incorporated into the calculation of the Casimir energy, offering a more realistic analysis of the force in multi-layer systems.

1.3.1 Fresnel Coefficients

Originally, Lifshitz obtained the closest expression for the plane-parallel geometry, known as the Lifshitz formula, for a system similar to the one illustrated in Figure 1.2b. In this setup, ε_l represents the dielectric function of the respective l material, where $l = 1$ and $l = -1$ correspond to the interacting plates, and $l = 0$ refers to the medium mediating the interaction. The distance between the semi-infinite bodies, or equivalently the thickness of the mediating material, is denoted by d, and $r_j^{(0,1)}$ and $r_j^{(0,-1)}$ represent the simple Fresnel reflection coefficients at the top and bottom interfaces of material $l = 0$ for polarizations $j = TE, TM$. One common form of the Lifshitz force expression at $T = 0\,\text{K}$ in such a system is given by:

In this expression, $\hbar$ is the reduced Planck constant and k_0 is the wavenumber component inside the mediating material, perpendicular to the interfaces. Additionally, k_0 is the wavenumber in the plane of the planar surface at the interface, perpendicular to $\mathbf{k}_\perp = (k_x, k_y)$. The expression for k_l is written as:

$$k_l = k_l(\omega, k_\perp) = \left[k_\perp^2 - \varepsilon_l(\omega)\frac{\omega^2}{c^2}\right]^{1/2} \tag{1.18}$$

The Fresnel reflection coefficients $r_{TM}^{(0,\pm1)}$ and $r_{TE}^{(0,\pm1)}$, are defined as:

$$r_{TM}^{(0,\pm1)}(\omega, k_\perp) = \frac{\varepsilon_{\pm1}(\omega)k_0 - \varepsilon_0(\omega)k_{\pm1}}{\varepsilon_{\pm1}(\omega)k_0 + \varepsilon_0(\omega)k_{\pm1}} \tag{1.19}$$

$$r_{TE}^{(0,\pm1)}(\omega, k_\perp) = \frac{k_0 - k_{\pm1}}{k_0 + k_{\pm1}} \tag{1.20}$$

The formal and derivation can be found in Appendix D for temperatures different than zero.

1.4 Topological Insulator

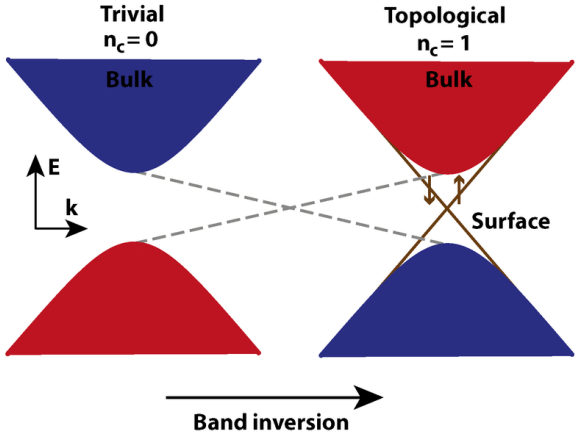

Figure 1.4: A topological insulator is a quantum state with an energy gap in the bulk but supports robust conductor surface states at the boundaries.

Materials are generally classified as insulators or metals based on their band structure. In 2007, however, a material that bend such classification was found: the first topological insulator, insulating in the bulk but conductive on the edges [20]. These unique states emerge from a delicate interplay of spin-orbit interactions and time-reversal symmetry. Within this framework, two-dimensional (2D) topological insulators manifest as quantum spin Hall insulators, akin to the inte-

ger quantum Hall state, while three-dimensional (3D) counterparts host intriguing spin-polarized 2D Dirac fermions on their surfaces [21]. Investigations into materials such as $Bi_{1-x}Sb_x$, Bi_2Se_3, Bi_2Te_3, and Sb_2Te_3 establish them as 3D topological insulators, directly probing the topology of their surface states [21]. Additionally, the discourse delves into the emergence of exotic surface states within 3D topological insulators spurred by induced energy gaps. These include a magnetic gap creating a new quantum Hall state and a superconducting gap supporting Majorana fermions, offering potential for topological quantum computation.

S.C. Zhang et al. proposed an alternative framework for understanding 3D topological insulators. In their model, the surface conductance is replaced by a quantized bulk linear magnetoelectric effect, referred to as topological magnetoelectric polarizability (TMEP) [22]. This concept is analogous to the hypothetical axion field suggested by particle physicists R. Peccei and H. Quinn [23], leading to the term axion insulators for 3D topological insulators; more about this can be found in Appendix H. The presence of the magnetoelectric effect significantly impacts vacuum fluctuations by altering the conventional Maxwell's boundary conditions, potentially affecting the Casimir interaction. In 2011, A. Gurshin et al. conducted a theoretical study on the impact of TMEP on the Casimir effect [24]. One of their most surprising predictions was the possibility of repulsive Casimir forces between two plates of topological insulators with opposite signs of the TMEP.

1.4.1 Parallel and Antiparallel Case

The magnetization direction can vary within the magnetic coatings applied to the layers of the Casimir system's topological insulator (TI) material. In this work, we will study two geometries, referred as parallel and anti-parallel. In the first one, the magnetization directions within the magnetic coatings on the TI layers are aligned in the same direction. This means that the magnetisation direction in each layer is consistent and points in the same direction. In contrast, in the antiparallel configuration, the magnetization directions within the magnetic coatings on the TI layers are opposite. This means that if you were to observe the direction of magnetization in each layer, you would find that they point in opposite directions [25]. These configurations are significant because they influence the overall magnetic properties of the system and, consequently, affect how the Casimir interaction behaves between the TI and normal insulator layers [25].

(a) (b)

Figure 1.5: (A) Antiparallel configuration: magnetizations in the magnetic coatings on the TI layers are opposite. (B) Parallel configuration: magnetizations in the magnetic coatings on the TI layers are aligned.

Chapter 2

Methods

2.1 Analytic Continuation

To determine the Casimir energy using Equation 1.11, it is necessary to have the reflection matrices at imaginary frequencies (refer to section 2.2). These reflection matrices can be obtained by solving Maxwell's equations and performing an analytic continuation to the imaginary axis in the complex frequency plane, where $\omega = i\xi$ [26].

$$\epsilon(i\hbar\xi) = 1 + \frac{2}{\pi}\int_0^\infty \frac{\hbar\omega\epsilon''}{(\hbar\omega)^2 + (\hbar\xi)^2} d(\hbar\omega) \tag{2.1}$$

Here, ϵ'' denotes the imaginary part of the permittivity at a frequency characterized by $\hbar\xi$. Due to experimental limitations, ϵ'' can only be determined within a finite energy range, $[\hbar\omega_1, \hbar\omega_2]$.
To accommodate this limitation, the integral is divided into three parts

$$\epsilon(i\hbar\xi) = 1 + \Delta_{\text{Low}}\,(\hbar\xi) + \Delta_{\text{Mid}}(\hbar\xi) + \Delta_{\text{High}}(\hbar\xi) \tag{2.2}$$

where $\Delta_{\text{Low}}\,(\hbar\xi)$ represents the contribution from frequencies below $\hbar\omega_1$, $\Delta_{\text{Mid}}(\hbar\xi)$ represents the contribution from frequencies within the range $[\hbar\omega_1, \hbar\omega_2]$ and $\Delta_{\text{High}}(\hbar\xi)$ represents the contribution from frequencies above $\hbar\omega_2$. Mathematically, these components are expressed as [27]:

$$\begin{aligned}
\Delta_{\text{Low}}\,(\hbar\xi) &= 1 + \frac{2}{\pi}\int_0^{\omega_1} \frac{\hbar\omega\epsilon''}{(\hbar\omega)^2 + (\hbar\xi)^2} d(\hbar\omega) \\
\Delta_{\text{Mid}}\,(\hbar\xi) &= 1 + \frac{2}{\pi}\int_{\omega_1}^{\omega_2} \frac{\hbar\omega\epsilon''}{(\hbar\omega)^2 + (\hbar\xi)^2} d(\hbar\omega) \\
\Delta_{\text{High}}(\hbar\xi) &= 1 + \frac{2}{\pi}\int_{\omega_2}^{\infty} \frac{\hbar\omega\epsilon''}{(\hbar\omega)^2 + (\hbar\xi)^2} d(\hbar\omega)
\end{aligned} \tag{2.3}$$

Given that our study focuses on insulators, we can state that the extrapolation for both low and high frequencies has been set to zero [28].

2.2 Transfer Matrix Method for Heterostructures in Electromagnetic Theory

Lifshitz's formula provides a framework applicable to heterostructures, although the challenge of computing the total reflection matrix, a task that involves solving for each reflection and transmission, often entailing complications [29].

The transfer-matrix method is widely used to analyze electromagnetic waves through stratified media, such as stacks of thin films [17]. In structures with multiple interfaces, as presented in Figure 2.1, reflections are partially transmitted and partially reflected multiple times.

The transfer-matrix method leverages Maxwell's equations, which dictate simple continuity conditions for the electric field across boundaries between different media. This principle allows for a straightforward computation: starting with the electric field known at the beginning of a layer, the field at the end of the layer can be derived using matrix operations [30]. By representing each layer with a transfer matrix and sequentially applying these matrices through the stack, the entire layered structure can be encapsulated within a system matrix [30] from which we can compute reflection and transmission coefficients straightforwardly.

$$
\begin{aligned}
[\mathbf{E}^{\mathrm{A}}] &= [T_{AB}][\mathbf{E}_i^{\mathrm{B}}] \\
[\mathbf{E}_i^{\mathrm{B}}] &= [P_B][\mathbf{E}_f^{\mathrm{B}}] \\
[\mathbf{E}_f^{\mathrm{B}}] &= [T_{BC}][\mathbf{E}_i^{\mathrm{C}}] \\
[\mathbf{E}_i^{\mathrm{C}}] &= [P_C][\mathbf{E}_f^{\mathrm{C}}] \\
[\mathbf{E}_f^{\mathrm{C}}] &= [T_{CD}][\mathbf{E}^{D}]
\end{aligned}
\tag{2.4}
$$

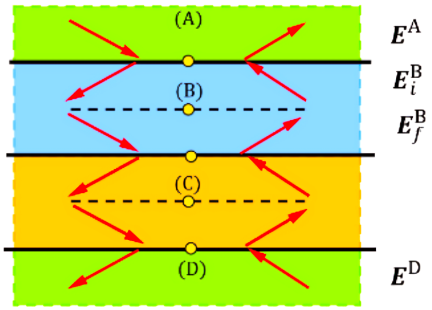

Figure 2.1: Multilayer configuration transmitted and reflected waves representation

The sequential equations governing this approach are described in Equation 2.4. It can be seen that the equations can be substituted into each other, leading to the following:

$$
\begin{aligned}
[\mathbf{E}^{\mathrm{A}}] &= [T_{AB}][\mathbf{E}_i^{\mathrm{B}}] \\
[\mathbf{E}_i^{\mathrm{B}}] &= [P_B][T_{BC}][P_C][T_{CD}][\mathbf{E}^{D}]
\end{aligned}
\tag{2.5}
$$

The latter can be further combined into a single matrix in the form:

$$
[\mathbf{E}^{\mathrm{A}}] = [T_{AB}][P_B][T_{BC}][P_C][T_{CD}][\mathbf{E}^{D}] \tag{2.6}
$$

or better written as:

$$
\left[E^{\mathrm{A}}\right] = [X_{AD}]\left[E^{D}\right] \tag{2.7}
$$

Here, E^{D} denotes the electromagnetic field in the reference medium and X_{AD} represents a simplified transfer matrix that relates the electromagnetic field (E^{A}) in the target medium (A) to the electromagnetic field (E^{D}) in the reference medium (D). This simplified matrix offers a more manageable representation than the comprehensive transfer matrix for heterostructures. Utilizing this decomposition, the transfer matrix for the electromagnetic field components, considering both s- and p-polarizations, can be depicted as

$$\begin{bmatrix} E_s^{A+} \\ E_s^{A-} \\ E_p^{A+} \\ E_p^{A-} \end{bmatrix} = \begin{bmatrix} X_{11} & \cdots & \cdots & X_{14} \\ \vdots & \ddots & & \vdots \\ \vdots & & \ddots & \vdots \\ X_{41} & \cdots & \cdots & X_{44} \end{bmatrix} \begin{bmatrix} E_s^{\mathrm{D}+} \\ E_s^{D-} \\ E_p^{\mathrm{D}+} \\ E_p^{D-} \end{bmatrix} \tag{2.8}$$

This matrix representation proves highly efficient in computing the heterostructure's total reflection matrix [25].

2.2.1 Medium Matrix

The medium matrix, denoted as **A**, provides an efficient method for computing the transfer matrix. It relates the amplitudes of modes to the tangential components of the electric and magnetic fields (E_x, E_y, H_x, H_y), which are crucial in defining boundary conditions [31]. The medium matrix simplifies and streamlines the analysis by expressing these conditions in terms of modes rather than direct field components and describes how incoming and outgoing field components transform. This transformation is fundamental for understanding how electromagnetic waves propagate through different heterostructure layers [32].

In electromagnetic theory, the electric field inside a medium can propagate in two distinct modes: s (transverse electric) and p (transverse magnetic). To construct the medium matrix **A**, we consider incoming ($+$) and outgoing ($-$) fields within the medium. The amplitudes of these modes and the corresponding field components are encapsulated in vectors γ^{A} and $\mathbf{f}^{\mathrm{A}}$, respectively.

In the absence of surface sources ($\sigma_f^s = 0$ and $j_f^s = 0$), it follows that

$$\begin{aligned} &(E^{\mathrm{A}} - E^{\mathrm{B}}) \times \hat{z} = \mathbf{0} \\ &(H^{\mathrm{A}} - H^{\mathrm{B}}) \times \hat{z} = \mathbf{0} \end{aligned} \iff \begin{cases} E_y^{\mathrm{A}} = E_y^{\mathrm{B}} \\ H_x^{\mathrm{A}} = H_x^{\mathrm{B}} \\ E_x^{\mathrm{A}} = E_x^{\mathrm{B}} \\ H_y^{\mathrm{A}} = H_y^{\mathrm{B}} \end{cases} \tag{2.9}$$

Furthermore, it follows that

$$\begin{aligned} [A] \left[\gamma^{\mathrm{A}}\right] e^{i\left(k_{\parallel} \cdot r_{\parallel} - \omega t\right)} = \left[f^{\mathrm{A}}\right] = \left[f^{\mathrm{B}}\right] = [B] \left[\gamma^{\mathrm{B}}\right] e^{i\left(k_{\parallel} \cdot r_{\parallel} - \omega t\right)} \\ \iff [A] \left[\gamma^{\mathrm{A}}\right] = [B] \left[\gamma^{\mathrm{B}}\right] \end{aligned} \tag{2.10}$$

where $[A]$ is the medium matrix, $\left[\gamma^{\mathrm{A}}\right]$ are the coefficients associated with each mode, and $\left[f^{\mathrm{A}}\right]$ are the field components in body A (with a similar definition for body B). Notice that the argument in the exponent is the same for both media and thus cancels out.
In summary, the mode coefficients of both media are related via their medium matrix. One can solve for the coefficients on one side by inverting the corresponding medium matrix

$$\left[\gamma^{\mathrm{A}}\right] = [A]^{-1}[B]\left[\gamma^{\mathrm{B}}\right] = [T_{AB}]\left[\gamma^{\mathrm{B}}\right]. \tag{2.11}$$

The matrix $[T_{AB}]$ receives the name of the transfer matrix and will play an important role in calculating the reflection coefficients.
Because we solved for the medium matrix for arbitrary complex ω and $k = (k_x, 0, k_z)$, the analytic continuation of the medium matrix $[M]$ at the imaginary axis is given by $\omega = i\xi$, where ξ is a positive real number. This implies [29] that:

$$k_z = \sqrt{\frac{-\xi^2\bar{\epsilon}\bar{\mu}}{c^2} - k_x^2} = i\sqrt{\frac{\xi^2\bar{\epsilon}\bar{\mu}}{c^2} + k_x^2} = i\tilde{k}_z. \tag{2.12}$$

Notice that $\tilde{k}_z$ is purely real and non-negative. It follows the medium matrix at the imaginary axis as follows

$$[M] = \left[\begin{array}{c|cccc} 1 & 1 & 1 & 0 & 0 \\ \tilde{k}_z\left(\mu_0\xi\bar{\mu}\right)^{-1} & 1 & -1 & 0 & 0 \\ -\tilde{k}_z c(\xi\sqrt{\epsilon\bar{\mu}})^{-1} & 0 & 0 & 1 & -1 \\ \sqrt{\bar{\epsilon}}\left(\mu_0 c\sqrt{\mu}\right)^{-1} & 0 & 0 & 1 & 1 \end{array}\right]. \tag{2.13}$$

2.3 Surface conductivity

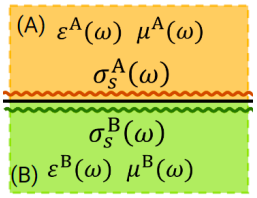

Figure 2.2: Interface condition between two media, described by the difference in surface conductivities, denoted by σ_s^{A} and σ_s^{B} respectively. The surface conductivity matrix $\sigma_S(\omega)$ is depicted as a 2x2 matrix, representing the conductivity components in the transverse direction.

The interface between two distinct materials introduces a set of conditions that govern the behaviour of electromagnetic fields, especially in topological insulators [21]. This is described by the interface condition

$$\begin{aligned} \left(H^{\mathrm{B}} - H^{\mathrm{A}}\right) \times \hat{n}^{\mathrm{AB}} &= j_s^f \\ &= j_s^{\mathrm{A}}(\omega) + j_s^{\mathrm{B}}(\omega) \end{aligned} \tag{2.14}$$

Here, the total current at the interface is the sum of contributions from both sides, denoted as $j_s^{\mathrm{A}}(\omega)$ and $j_s^{\mathrm{B}}(\omega)$. The generalized Ohm's law provides further insight into the surface conductivity [6]

$$\begin{aligned}\left(H^{\mathrm{B}} - H^{\mathrm{A}}\right) \times \hat{n}^{\mathrm{AB}} &= j_s^f \\ &= \sigma_s^{\mathrm{A}}(\omega) \cdot E_k^{\mathrm{A}} + \sigma_s^{\mathrm{B}}(\omega) \cdot E_k^{\mathrm{B}}\end{aligned} \tag{2.15}$$

This equation introduces the surface conductivities $\sigma_s^{\mathrm{A}}(\omega)$ and $\sigma_s^{\mathrm{B}}(\omega)$, characterizing the material-specific response at the interface. The surface conductivity is represented as a matrix

$$\sigma_S(\omega) = \begin{bmatrix} \sigma_{xx}(\omega) & \sigma_{xy}(\omega) \\ \sigma_{yx}(\omega) & \sigma_{yy}(\omega) \end{bmatrix} \tag{2.16}$$

where $\sigma_{xx}(\omega)$ and $\sigma_{yy}(\omega)$ represent the longitudinal conductivity, while $\sigma_{xy}(\omega)$ and $\sigma_{yx}(\omega)$ are the Transverse Hall conductivity. For in-plane isotropic samples, the conditions $\sigma_{xx} = \sigma_{yy}$ and $\sigma_{xy} = -\sigma_{yx}$ hold true.

Surface conductivity modifies the medium's matrix by adding a dependence on the parameter $\theta = (2n+1)\pi$. This modification leads to the quantized topological magnetoelectric polarizability (TMEP) adopted in this study. An important consideration is that θ depends on the frequency, which limits the model described above. Nonetheless, this frequency dependence remains an active area of research [33]. Another way to recover the TMEP is using Quantized bulk linear magneto-electric as explained in section H.1.

2.3.1 Toy Model: Lorentz Oscillators

A. Gurshin et al.'s analysis of the Casimir force between topological insulators (TIs) relies on several simplifications [24]. Firstly, they overlook the attractive Casimir force between magnetic layers, suggesting an insulating ferromagnetic layer to mitigate this effect. However, this approach complicates force measurements due to electrostatic corrections. Secondly, they model the dielectric response of TIs using Lorentz oscillators, which fail to capture the non-zero bulk conductivity present in many TI samples due to dislocations, impurities, and thermal excitation [34]. Consequently, the impact of more realistic models on repulsive forces remains unknown. Initially, Gurshin et al. assumed a frequency-independent topological magnetoelectric polarization (TMEP). Later, they propose a frequency-dependent surface conductivity for a more accurate description of the Casimir effect between TIs. In 2014, they predicted repulsive forces at larger separations and attractive forces at smaller separations between two Chern insulators, making stable levitation impossible. However, the effects of frequency-dependent surface conductivity on repulsive forces between 3D TIs have not been thoroughly studied.

We now introduce the simplified model, which employs a single Lorentz oscillator. This model

describes the dielectric response as follows [24]:

$$\bar{\epsilon}(\omega) = 1 + \frac{\omega_A^2}{\omega_0^2 - \omega^2 - i\gamma\omega} \quad \bar{\epsilon}(i\xi) = 1 + \frac{\omega_A^2}{\omega_0^2 + \xi^2 + \gamma\xi}, \tag{2.17}$$

Here, ω_A, ω_0, and γ represent the amplitude-frequency, natural frequency, and dissipation respectively. Replacing ω with $i\xi$ facilitates the transition to imaginary frequencies. In this study, we consider the topological insulator (TI) to be non-magnetic ($\bar{\mu}^{\mathrm{B}} = 1$), and we simplify the gap medium (A) as vacuum ($\bar{\mu}^{\mathrm{A}} = 1$) [35].

To underscore the practical implications of our findings, we construct a simplified model based on $\mathrm{TlBiSe_2}$ [36]. Available literature shows this material exhibits a natural frequency of approximately $\hbar\omega_0 \sim 6.58\mathrm{meV}$. Previous research indicates that dissipation minimally affects the Casimir force, hence we set $\gamma = 0.01\omega_0$ [37]. Considering the inverse relationship between static permittivity and equilibrium distances, we choose $\omega_A = 0.45\omega_0$. The permittivity and its analytical continuation for this model are depicted in Figure 2.3a, Figure 2.3b.

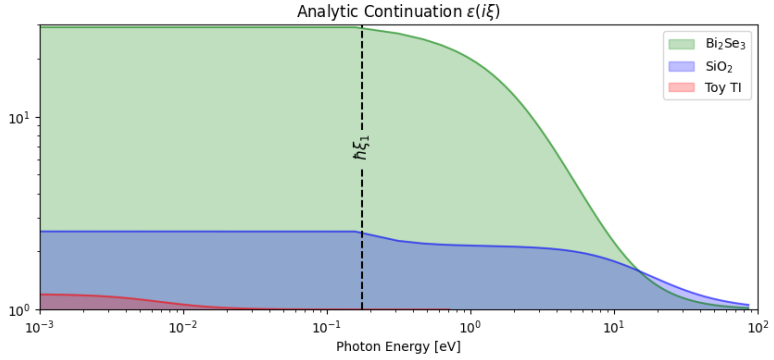

(a)

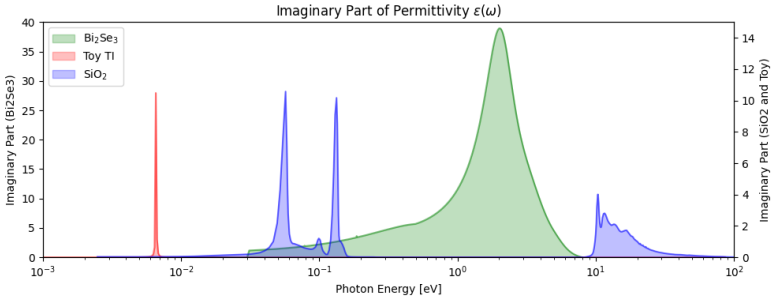

(b)

Figure 2.3: (A) Permittivity at imaginary frequencies, no extrapolation is needed for insulators. (B) Exploring the Imaginary Permittivity: $\mathrm{Bi_2Te_3}$ on the left, $\mathrm{SiO_2}$ & Toy TI on the right.

A particularly useful method for representing the forces between different values of TMEP is to compare them with the force experienced by the topologically trivial phase, in this way, we can gauge the effects of surface conductivity in the total force. We define the topological force contrast

(TFC) as follows:

$$\mathrm{TFC}(d) = \frac{F_{\mathrm{sp}}\left(d; n_1, n_2\right)}{F_{\mathrm{sp}}(d; 0{,}0)} \tag{2.18}$$

where $F_{\mathrm{sp}}\left(d; n_1, n_2\right)$ is the sphere-plate force at distance d for TMEPs given by $(n_{,n_2)}$. This result is noteworthy as it is independent of the sphere's radius.

2.3.2 Vacuum - Toy Model system as a Baseline for Future Comparisons

A simple system, consisting of a first layer of vacuum and a second layer of a topological insulator (TI) with conductivity in the middle, is used to establish a baseline for future comparisons. The Topological Force Contrast (TFC) and Reduction factor are calculated for different conductivity values in configurations with opposite n_2 values.

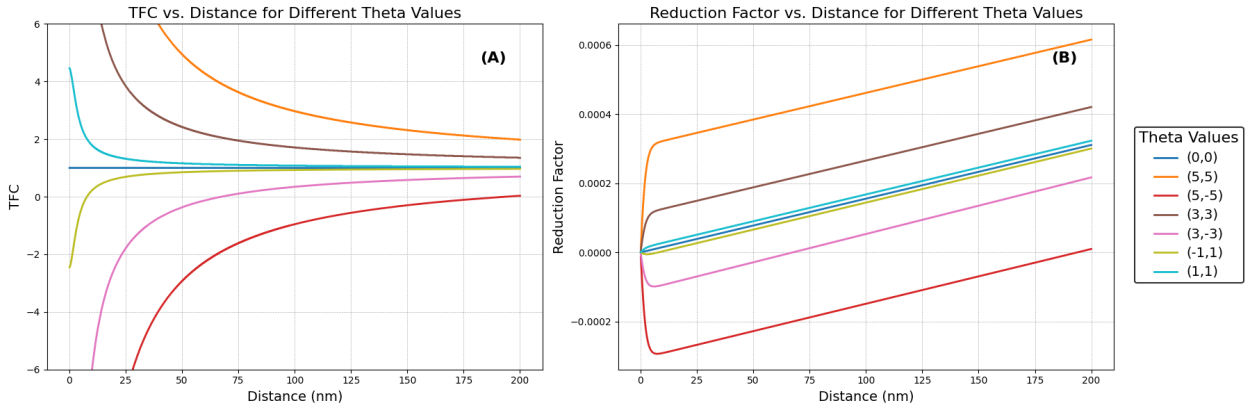

Figure 2.4: (A) Topological Force Contrast (TFC) for Varying Theta in a Toy Model with Fixed Parameters B=4nm and C=10nm. (B) Reduction Factor for the Toy Model with Varying Conductivity

In Figure 2.4, the force values for some θ configurations present negative TFC values corresponding to a levitation effect on the material. Essentially, as the conductivity varies, the forces acting on the material increase, indicating that the material might experience a lifting force strong enough to counteract gravity, leading to levitation.
Future calculations in this thesis will try to substitute real topological insulator materials like Bi_2Se_3 in different configurations, attempting to determine if levitation is also possible.

2.3.3 Bi_2Se_3 with Surface Conductivity: Simplest Case

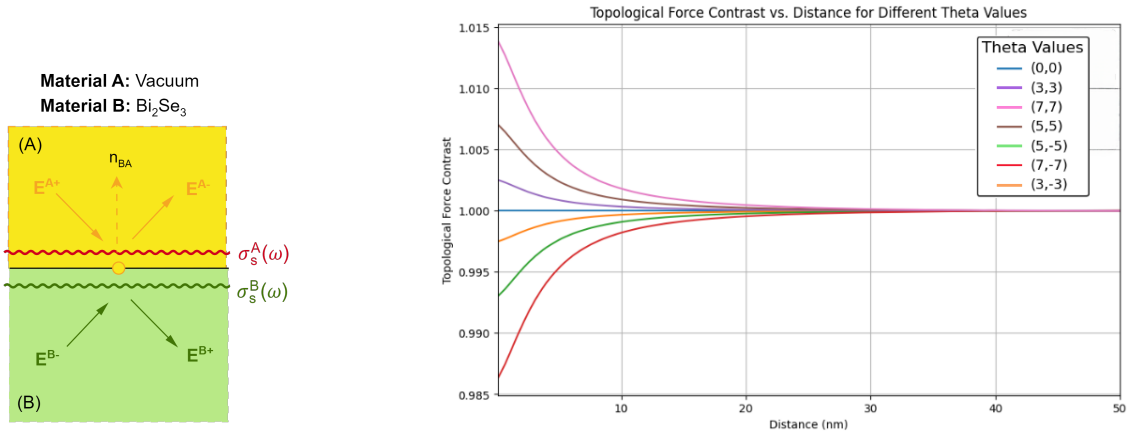

(a) (b)

Figure 2.5: (A) Material A (Vacuum) and Material B with conductivity profiles. (B) Topological Force Contrast (TFC) for a two-layer system in which Bi_2Se_3 is the Material B.

We analyzed the influence of different theta values on the Topological Force Contrast (TFC). For subsequent values of theta involved in the first 25nm, a change of approximately 1.5%, the results are shown Figure 2.5b. Bi_2Se_3 TFC decreases with distance for all theta values, with the effect being more pronounced for larger theta values.

2.3.4 Comparative Analysis

The simple toy model case, depicted in Figure 2.4, shows that a great difference in TFC values suggests a substantial variation in force profiles—values of 2 indicate a 200% difference, illustrating a significant disparity in force; however, real material exhibits a more modest 1% contrast. Our ongoing work aims to explore strategies for increasing this contrast, such as employing liquid gaps and multilayers. These approaches are crucial for understanding how surface properties, like conductivity, can be tailored to manipulate the magnitude and nature of Casimir force. Furthermore, in realistic scenarios, the disappearance of repulsive forces and the reduction in TFC underscore the complexity of real material interactions compared to idealized models like the toy model.

2.4 Oscillator Model at Different Frequencies

Simple oscillators are valuable for parameterizing dielectric functions, particularly at imaginary frequencies for liquid gaps. This section explores the application of oscillator models to comprehensive dielectric data derived using the Kramers-Kronig method [1]. The classical oscillator model, as described in [38], represents the dielectric function at imaginary frequencies as follows:

$$\varepsilon(i\zeta) = 1 + \sum_i \frac{C_i}{1 + (\zeta/\omega_i)^2} \tag{2.19}$$

where C_i denotes the strength of an oscillator associated with a specific resonance frequency ω_i. We employ this model to fit the dielectric functions obtained through the aforementioned method. This approach facilitates the application of Lifshitz's theory for Casimir force calculations. The extensive frequency range covered by the measured dielectric data significantly enhances the accuracy of these oscillator representations [39]. For most materials, the constructed oscillator models are valid within the frequency range of 10^{-2} to 10^{2} eV. This range includes the first infrared (IR) Matsubara term, which is essential for finite-temperature force calculations. It is important to note that, unlike solids, where sample dependence necessitates using two sets of dielectric data, liquids are not expected to exhibit such variations. Therefore, a single data set is sufficient for constructing oscillator models for liquids. Using this assumption, Ninham and Parsegian obtained a simplified expression for $\epsilon(i\omega_n)$ as [40]:

$$\epsilon(i\omega_n) = 1 + \frac{\epsilon_\infty - \epsilon_0}{1 + \omega_n/\omega_{\mathrm{MW}}} + \frac{\epsilon_0 - n_0^2}{1 + (\omega_n/\omega_{\mathrm{IR}})^2} + \frac{n_0^2 - 1}{1 + (\omega_n/\omega_{\mathrm{UV}})^2} \tag{2.20}$$

where ϵ_∞ is the static dielectric constant, ϵ_0 is the dielectric constant when the microwave relaxation ends and the infrared relaxation begins, n_0 is the refractive index in the visible range, and $\omega_{\mathrm{MW}}, \omega_{\mathrm{IR}}$, and ω_{UV} are the characteristic microwave, infrared, and ultraviolet absorption frequencies.

[1] The Kramers-Kronig relations enable the determination of the refractive index profile and chromatic dispersion of a material using only its frequency-dependent absorption losses, which can be measured across a wide spectral range.

Chapter 3

Casimir Effect in Liquid Gaps

Liquid gaps have previously been associated with repulsive forces. The question now arises whether such liquid gaps could potentially increase the TFC. In this section, we focus on examining the impact of fluid permittivity on the forces involved. Utilizing Equation 2.20 and the real material data presented in [41], [42], we analyze how variations in liquid permittivity influence these forces.

Table 3.1: Dielectric Dispersion Data and Spectroscopic Constants of Methanol, Glycerol, and Water

Material	ϵ_∞	ϵ_0	ω_{MW} (rad/s)	n_0^2	$\omega_{\text{IR}} \times 10^{-14}$ (rad/s)	$\omega_{\text{UV}} \times 10^{-16}$ (rad/s)
Methanol	33.64	5.7	1.88×10^{10}	1.7349	3.52	1.87
Glycerol	42.5	4.16	8×10^{8}	2.136	3.28	1.895
Water	80.1	5.2	1.06×10^{11}	1.755	5.66	1.793

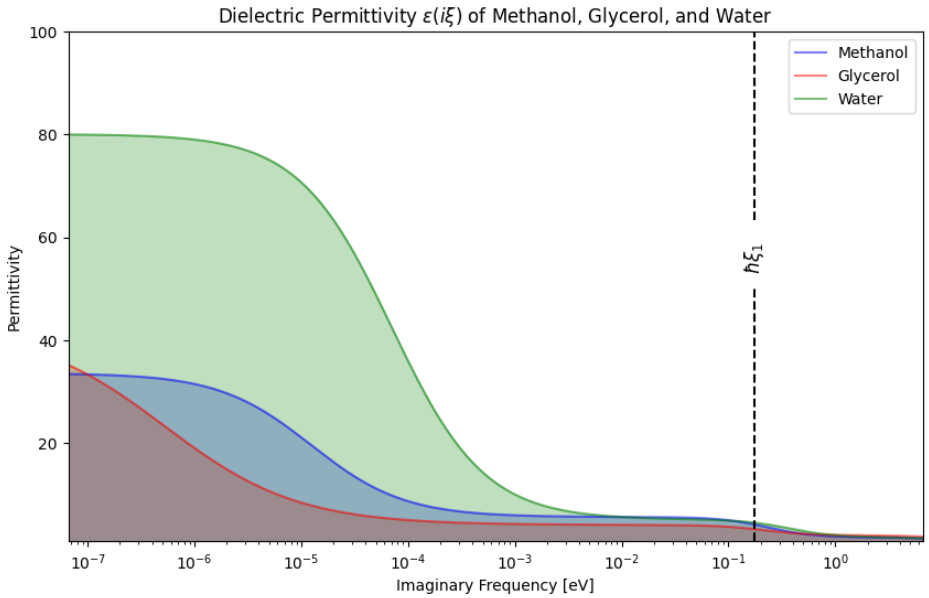

Figure 3.1: Plot showing the dielectric permittivity $\epsilon(i\omega_n)$ of Methanol, Glycerol, and Water as a function of the imaginary frequency. The dielectric permittivity is calculated using the simplified model considering contributions from microwave, infrared, and ultraviolet relaxations.

3.1 Conductivity in Liquids

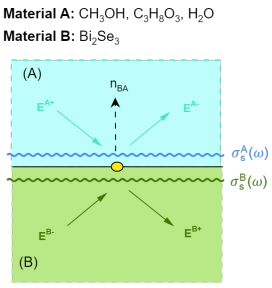

Figure 3.2: Visualization of two distinct materials: (A) composed of CH_3OH, $C_3H_8O_3$, H_2O, and (B) Bi_2Se_3. Arrows depict the propagation of electric field, while ellipses signify surface electronic states.

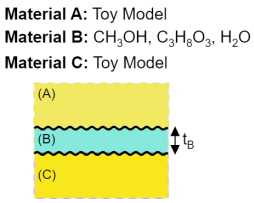

Figure 3.3: Comparison of dielectric responses between different materials: Material A (toy model), Material B (CH_3OH, $C_3H_8O_3$, H_2O), and Material C (toy model).

The effects of a fluid gap in the Casimir forces in the presence of surface conductivity are crucial for studying Casimir forces in liquid-solid systems. In this context, the dielectric properties of the intervening liquid medium are essential. The dielectric constant of the liquid significantly influences the magnitude and nature of the Casimir force between two closely spaced surfaces immersed in the liquid.

3.1.1 Toy Model for Enhancement of Repulsive Casimir Force

In our study, we examine the behaviour of a Lorentz oscillator, a simplified model often used to describe the dielectric response. We will now focus on systems as the one described in Figure 3.3 where the two other layers are described by the toy model and the inner layer is a liquid one. Figure 3.4 illustrates that the TFC values never exhibit negative values, corresponding to the levitation case, thus more closely resembling real materials.

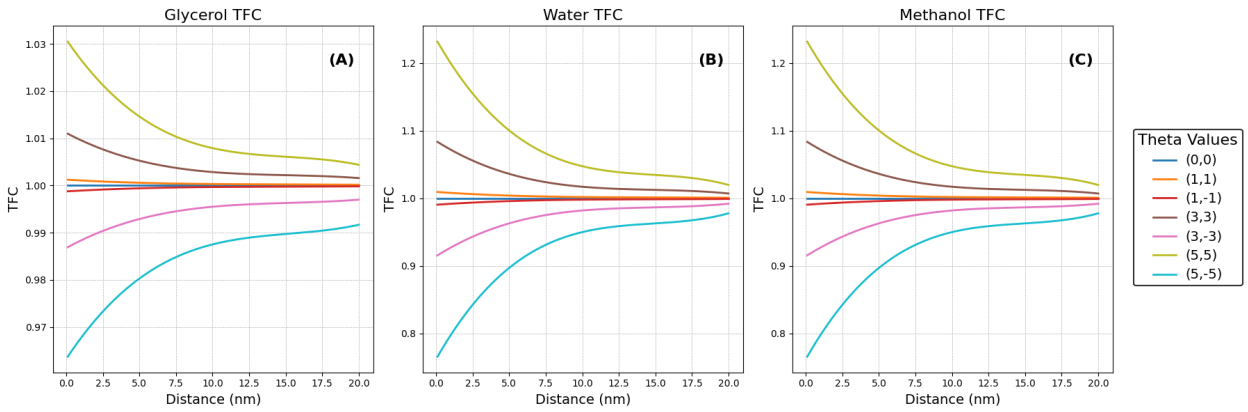

Figure 3.4: (A) TFC Glycerol-Toy Model. (B) TFC Water-Toy Model. (C) TFC Methanol-Toy Model.

The toy model predicts that the TFC should decrease with increasing distance and that the TFC for water should be greater than the TFC for methanol or glycerol. These predictions contradict the one reported for the single Toy model structure presented in Figure 2.4, anyway in Figure 3.4, the impact of θ values on the TFC is consistently observed across methanol, glycerol, and water.

3.1.2 Real Material Behaviour

We analysed the influence of different θ values on the Topological Force Contrast (TFC) for glycerol, water, and methanol for the system described in Figure 3.2, where Bi_2Se_3 is used as first layer. To achieve this, we calculated the percentage contribution of each θ value to the total TFC for each liquid.

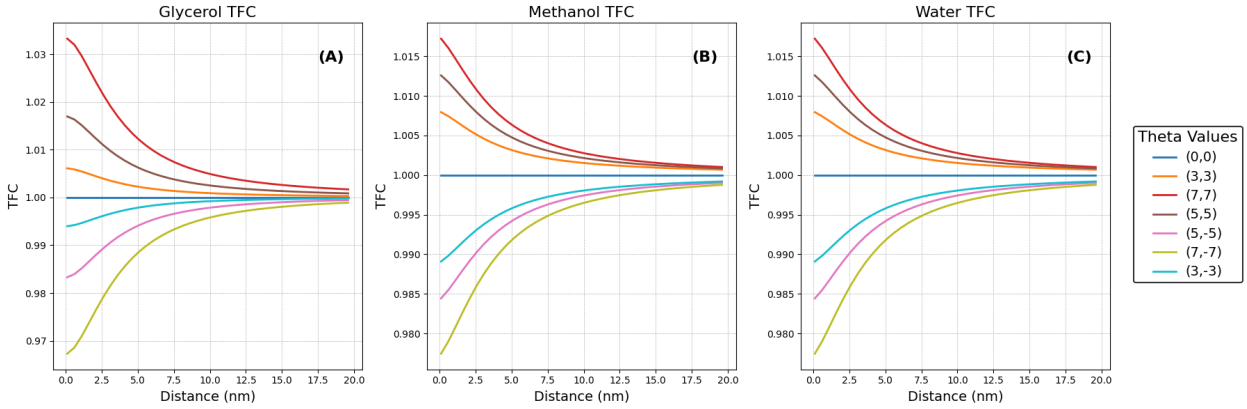

Figure 3.5: Topological Force Contrast (TFC) for Glycerol, Methanol and Water using the schematics presented in Figure 3.2

.

For Water and Methanol, a change between subsequent values of θ involves a change of approximately 1.4% in the first 2.5 nm, while for Glycerol, the decrease is in the same range, roughly 2.0%.

3.2 Analysis of Topological Force Contrast Data

The impact of θ values on the topological force contrast is consistent in all three media (methanol, glycerol, and water). Positive θ values lead to an initial increase in the TFC, whereas negative θ values result in an initial decrease. This pattern indicates a uniform response to θ variations across different media. Glycerol exhibits the most significant range of TFC values, suggesting that the properties of this medium greatly influence the extent of TFC variation. Methanol and Water, on the other hand, show a similar range of TFC values. However, Water displays a sharper initial divergence, highlighting a more pronounced response at the onset of the interaction.
As the distance increases, the TFC in all three media approaches 1. This asymptotic behaviour indicates that, regardless of the medium, the TFC's long-range behaviour remains consistent. This

convergence to unity suggests that the surface conductivity effects are negligible at larger distances. We performed pairwise t-tests to compare the means of the TFC data between each pair of liquids corresponding to the same values of θs, to assess whether the means of two groups are statistically different, as differences in TFC could reflect variations in physical properties such as viscosity, density, or molecular interactions in the realm of Casimir Force measurements. More detailed results and discussions on these comparisons can be found in Appendix I.

3.2.1 Data Comparison

The toy model shows a more pronounced separation between the positive and negative θ values than the real material results. Water, in particular, demonstrates a sharper initial divergence in both cases, reinforcing the idea of a distinct response to θ variations at short distances. In the real material results and the toy model, the TFC approaches 1 as the distance increases, indicating a consistent long-range behaviour regardless of the medium. While both sets of figures demonstrate similar overall trends, there are differences in the magnitude and rate of change of TFC values. The toy model's separation between the curves for different θ values appears more pronounced, especially at shorter distances. This could suggest that the toy model exaggerates certain effects seen in the real material data or that it captures some idealized aspects of the system not present in the real-world measurements. Overall, the comparative analysis between the real material results and the toy model highlights consistent trends in the impact of θ values, medium dependency, and asymptotic behaviour of TFC. Both approaches confirm that Glycerol exhibits the most significant TFC variations. The toy model provides a useful, though slightly exaggerated, representation of the real material phenomena, with an enhancement of almost 20% if the surface states are considered, the effects are anyway visible only in a short distance range. A last consideration is that the TFC for Bi_2Se_3 increased compared with the vacuum case, but very little.

Chapter 4

Multilayers with Free Parameters

4.1 Three Layers with Varying Thickness of Middle Layer

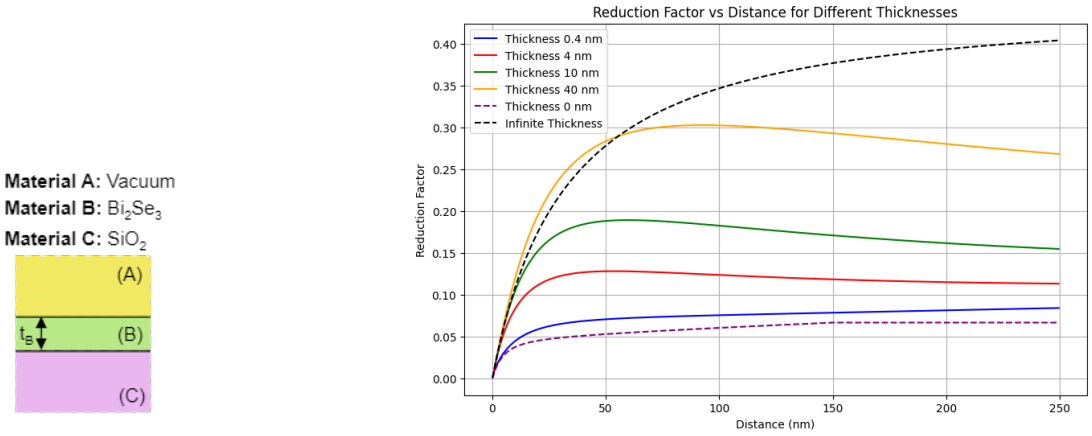

(a) (b)

Figure 4.1: (A) Materials Slab: (a) Vacuum, (b) Bi_2Se_3, (c) SiO_2. The diagram illustrates the interface between these materials, highlighting their distinct boundaries and interfaces. The parameter to be changed is the thickness of the middle layer. (B) Reduction Factor across Various Thicknesses of a Stack as described in A.

4.1.1 Reduction Factor

The influences of different thicknesses of Bi_2Se_3 on the reduction factor can be seen in Figure 4.1. It can be seen that there is an increasing trend for all thicknesses except for 0 nm and infinite thickness.

It is evident that the reduction factor values fall between those of the two limiting cases: one with infinite thickness (indicating the presence of Bi_2Se_3) and the other with zero thickness (indicating the absence of Bi_2Se_3). This suggests that the observed system includes Bi_2Se_3, but there are no enhancements in the reduction factors beyond the expected range set by these limits, apart from the thickness of 40 nm in a very short range of distances.

Our calculations assume no change in the electronic properties (specifically the dielectric constant,

ϵ) with thickness. However, this assumption is inaccurate for topological insulators (TIs), like Bi_2Se_3, where the surface states mix and can significantly alter the electronic properties. This factor should be considered for a more accurate representation of the system.

4.1.2 Toy model comparison

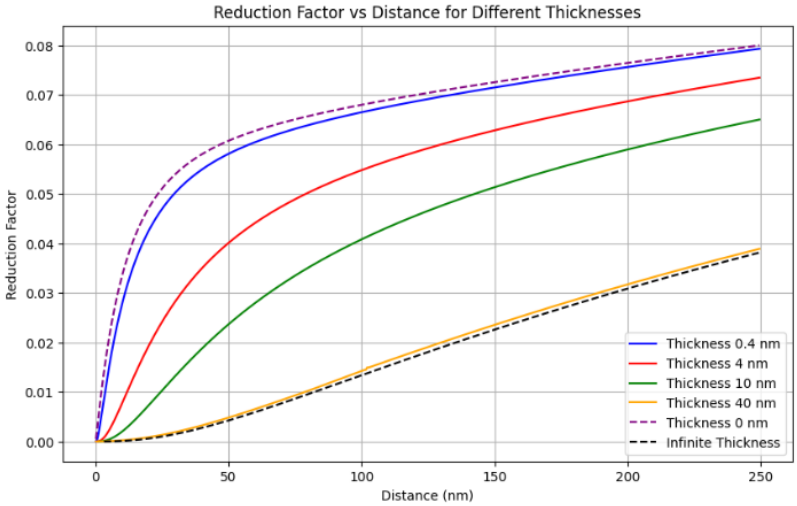

Figure 4.2: Reduction Factor across Various Thicknesses of the Middle Layer in a Stack Comprising Vacuum, Toy Model, and Silicon Oxide.

Figure 4.2 reveals that the reduction factor is significantly influenced by the thickness of the middle layer. Thinner layers provide a higher reduction factor at shorter distances, while thicker layers show a more gradual increase over a longer distance range in agreement with other studies [32], [43]. The infinite thickness scenario sets an upper bound for reduction effectiveness; zero thickness represents minimal reduction.

The comparative analysis reveals that the type of material in the middle layer significantly affects the reduction factor's behaviour. In the first stack (vacuum, toy model, and SiO_2), the reduction factor consistently increases and plateaus at long distances, especially for thicker layers. In contrast, the second stack (vacuum, Bi_2Se_3, and SiO_2) exhibits a more dynamic response, with thicker layers showing a peak and decline, indicating that Bi_2Se_3 introduces complex interactions affecting the reduction factor over distance. This highlights the critical role of the middle layer material in determining the overall reduction behaviour in multilayer stacks.

In contrast to the Bi_2Se_3 case, the reduction factor is highest for the thinnest layer (0.4 nm) and decreases with increasing thickness, reaching its lowest point for infinite thickness.

4.2 N Layers with Varying Thickness of Each Layer (Except the First One)

In this step, our analysis becomes more intricate as we extend the system to N layers, where N is a variable[1]. The mathematical model is adapted to accommodate multiple layers, and the thickness of each layer, except the first, corresponds. This configuration allows us to explore the collective impact of layer thickness variations on the Casimir force and reduction factor.

4.2.1 Calculations for repetition N=2 of 3 Layers

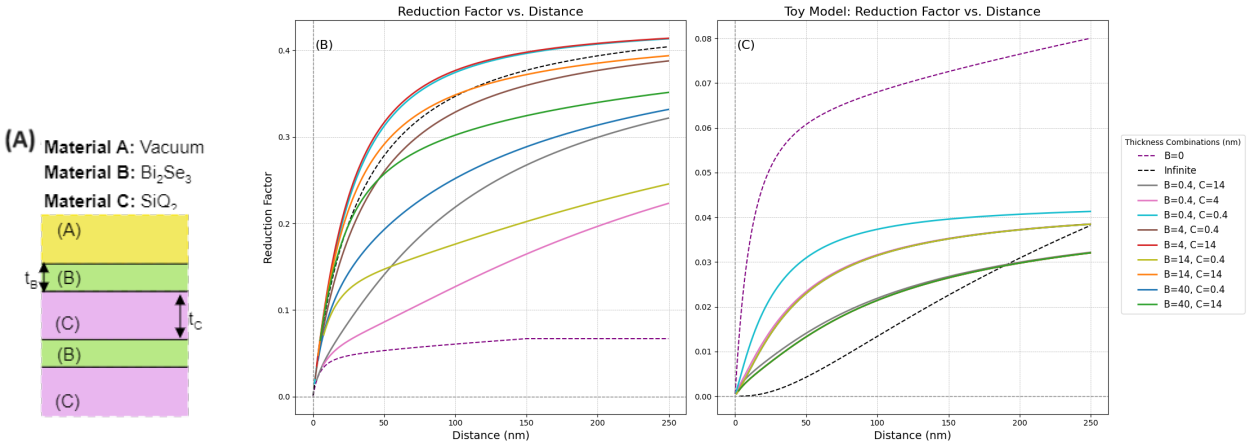

Figure 4.3: (A) Layered heterostructure composed of Vacuum (A), Bi_2Se_3 (B), and SiO_2(C) with corresponding layer thicknesses denoted as t_B and t_C, repetition of the layers twice. (B) Repetition of 3 layers twice: Reduction factor for different combinations of the thicknesses of Layer B and C. (C) Reduction Factor where Layer B is the Toy model

The reduction factor for the systems was calculated as shown in Figure 4.3. For the Bi_2Se_3 case, it can be seen that for the short-range between 30 and 100 nm, there is an enhancement in the force for the configurations with B=14 nm and C=14 nm. Additionally, the configurations with B=4 nm and C=14 nm and B=40 nm and C=14 nm show force enhancement over a longer range. Therefore, it can be concluded that in this configuration, a substrate thickness of 14 nm enhances the force, unless the bulk thickness is too large (as in the 40 nm case).
For the toy model, on the other hand, the only case in which the force improves, and only at very large distances, is when the toy model itself is very large, as seen with the B=40 nm line. However, this configuration follows a similar trend to the B=0.4 nm and C=14 nm configurations, so no clear trend can be deduced.

[1] The number of layers refers to the layers of TI, but the last layer is always the substrate.

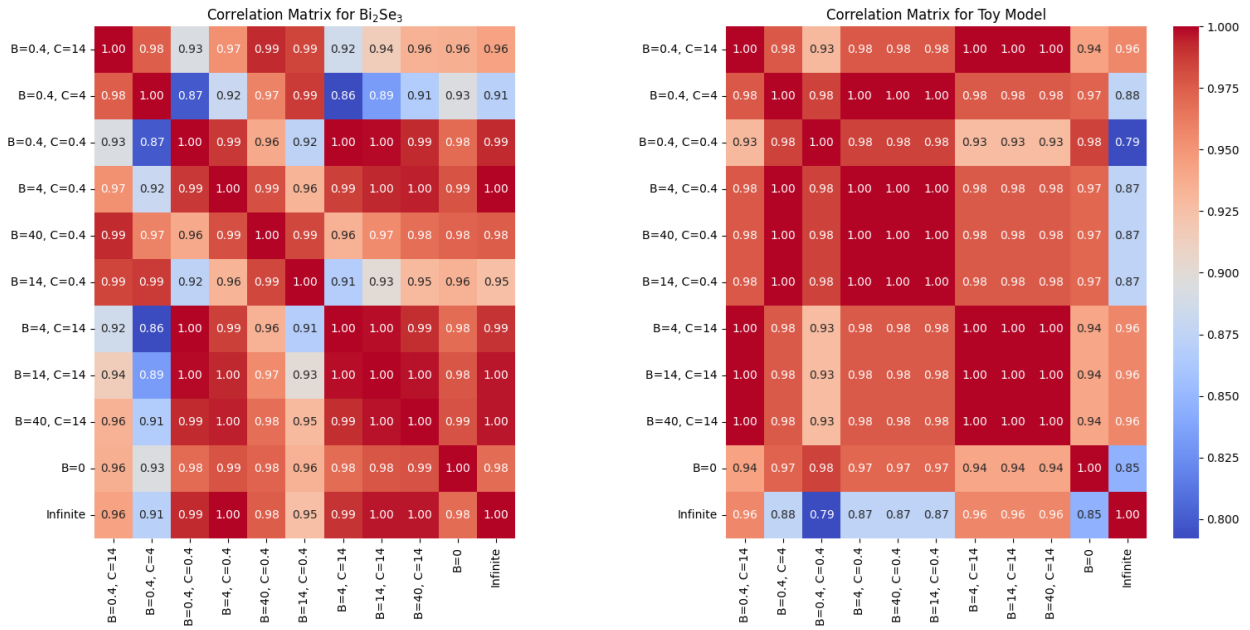

Figure 4.4: Correlation matrix N=2 repetition comparison.

The Figure 4.4 presents a correlation matrix that illustrates the correlation coefficients between various thickness combinations of layers B and C in a multilayer system with $N = 2$ repetition. These matrices provide insights into the interaction patterns of the Casimir force reduction factor for both Bi_2Se_3 and a simplified toy model. The analysis aims to determine whether the thickness of the middle gap plays a crucial role in the behaviour of the reduction factor over distance.

A general trend observed is that areas with the highest correlation correspond to similar thicknesses of the second layer. In the correlation matrix for Bi_2Se_3, high correlation pairs include $B = 0.4\,\text{nm}, C = 14\,\text{nm}$ and $B = 4\,\text{nm}, C = 14\,\text{nm}$, $B = 0.4\,\text{nm}, C = 4\,\text{nm}$ and $B = 4\,\text{nm}, C = 4\,\text{nm}$, and $B = 14\,\text{nm}, C = 0.4\,\text{nm}$ and $B = 14\,\text{nm}, C = 4\,\text{nm}$ with a correlation of 0.99. These high values indicate that the reduction factors for these combinations behave very similarly over the observed distance range.

On the other hand, moderate to low correlation pairs can be seen in combinations like $B = 0.4\,\text{nm}, C = 4\,\text{nm}$ and $B = 40\,\text{nm}, C = 0.4\,\text{nm}$. A general trend is that layers with $B = 0.4\,\text{nm}$ generally show high correlations with both thin and thicker layers like $C = 14\,\text{nm}$.

The correlation matrix for the toy model shows similar high correlation values, particularly in configurations like $B = 0.4\,\text{nm}, C = 14\,\text{nm}$, $B = 4\,\text{nm}, C = 14\,\text{nm}$, $B = 0.4\,\text{nm}, C = 4\,\text{nm}$, and $B = 4\,\text{nm}, C = 4\,\text{nm}$ with a correlation of 0.98. However, distinct low correlation pairs, such as $B =$ Infinite and $B = 0.4\,\text{nm}, C = 14\,\text{nm}$, show a moderate correlation of 0.79. Both thin and thick layers in the toy model show high correlations with various thickness combinations, indicating a uniform response in the reduction factor across different distance ranges.

The comparative analysis underscores the importance of layer thickness in determining the Casimir force in multilayer systems. The high correlation values in both Bi_2Se_3 and toy model systems indicate that certain thickness combinations can be optimized for desired Casimir force properties,

providing valuable insights for applications in nanotechnology and materials science.

4.3 Three Layers with Surface Conductivity on Both Top and Bottom of Middle Layer

In this step, the complexity of our analysis increases as we introduce surface conductivity not only to one or both layers but specifically on the top and bottom surfaces of the middle layer in a three-layer system. This modification explores the combined effects of layer thickness and surface properties on the Casimir force.

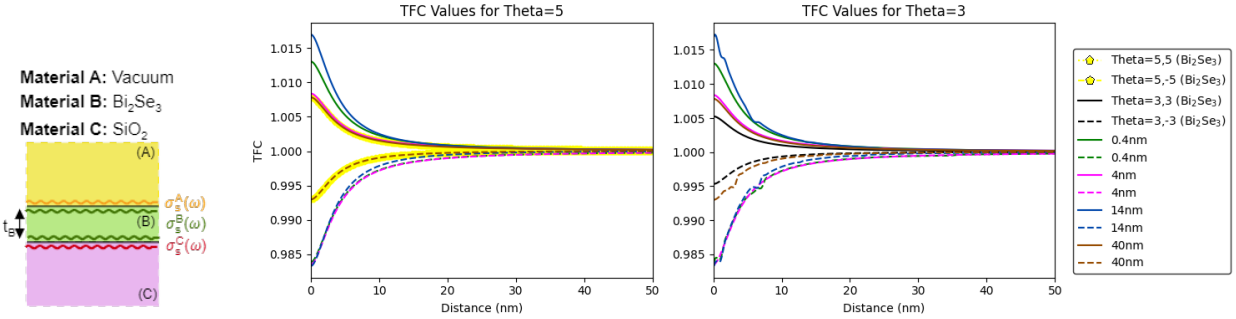

Figure 4.5: (A) Layered heterostructure composed of Vacuum (A), Bi_2Se_3 (B), and SiO_2(C). Layer thicknesses are denoted as t_B, and surface conductivity is present. (B) Topological Force Contrast as a Function of Distance for two Theta Values for a three-layer system described in A, the dotted lines correspond to the oppositely oriented n_1 and n_2 of the TFC.

Notably, the data suggests that theta does not influence the reduction factor; variations are observed solely based on thickness, which can be particularly observed in the TFC graph. Furthermore, for the same thickness, all lines overlap, indicating consistent behaviour across the sampled range. T-test and Anova Test for statistical analysis of the results are reported in Appendix J.
In both cases, an enhancement of the force is presented, as some cases present higher TFC than the corresponding two-layer case presented in Figure 2.5b. In particular, for $\theta = 5$, the thicknesses of 0.4 nm and 14 nm for Bi_2Se_3 present a 0.5% enhancement, while for $\theta = 3$ all combinations present better results.

4.3.1 Comparative Analysis with Previous Steps

Surface conductivity alters the electromagnetic properties of the material surfaces, leading to modifications in the dispersion relations and, consequently, the Casimir force. Particularly in a three-layer system where surface conductivity is present on both the top and bottom surfaces of the middle layer, these alterations can manifest as changes in the magnitude and spatial distribution of the Casimir force. The interplay between surface conductivity and layer thickness further compli-

cates the scenario, as variations in one parameter can exacerbate or mitigate the effects of the other, ultimately negatively influencing the reduction factor of the Casimir force.

4.3.2 Comparison with Toy Model

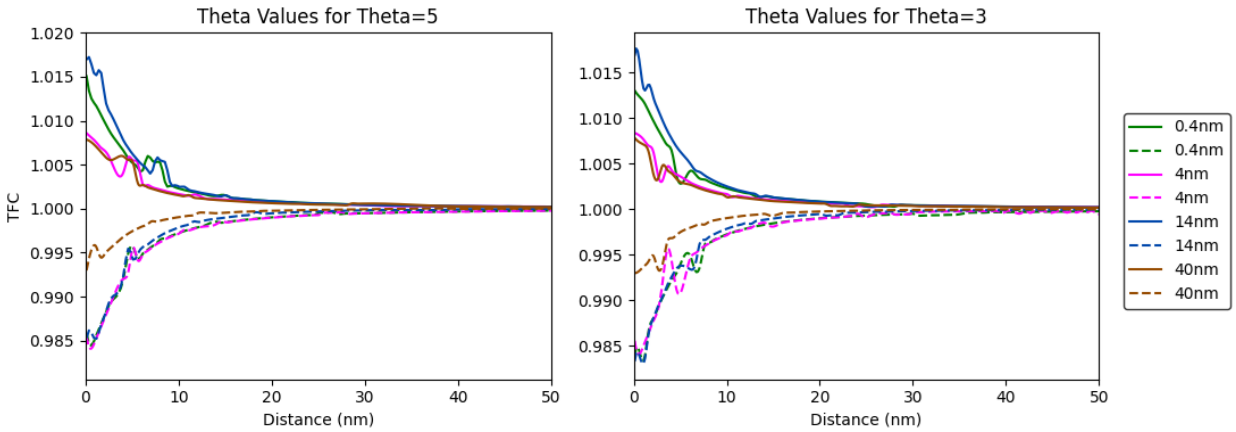

Figure 4.6: Topological Force Contrast as a Function of Distance for two θ Values for a three-layer system, where the middle layer is now the toy model.

Similar to Figure H.2b, the TFC initially varies with distance and stabilizes. This consistent pattern across different configurations underscores the importance of distance in achieving a stable TFC. Different thicknesses at θ=(5,5) (0.4 nm, 4 nm, 14 nm, 40 nm) exhibit significant initial variations in TFC values. However, despite these initial differences, all curves stabilize around a TFC value of 1.000 after a distance of 30-40 nm. None of them presents an enhancement of the TFC, as they are both bounded by the values presented in Figure 2.4 nor levitation, as the reduction factor did not present trends similar to the rising ones presented in Figure 2.4. In particular, the TFC was not plotted, as for the simple Toy model case, the values ranged from -7 to 7, making all the other values in the graph not visible anymore. We can, therefore, conclude that the Toy model significantly reduces the Force in this multi-layer structure.

4.3.3 Extending Dual-Sided Surface Conductivity to N Layers

In this final step, we extend the complexity introduced in the above subsection to a multilayer system with N layers, incorporating dual-sided surface conductivity on the middle layer. The mathematical model is adapted to accommodate multiple layers, each with the potential for surface conductivity on both the upper and lower surfaces of the middle layer.

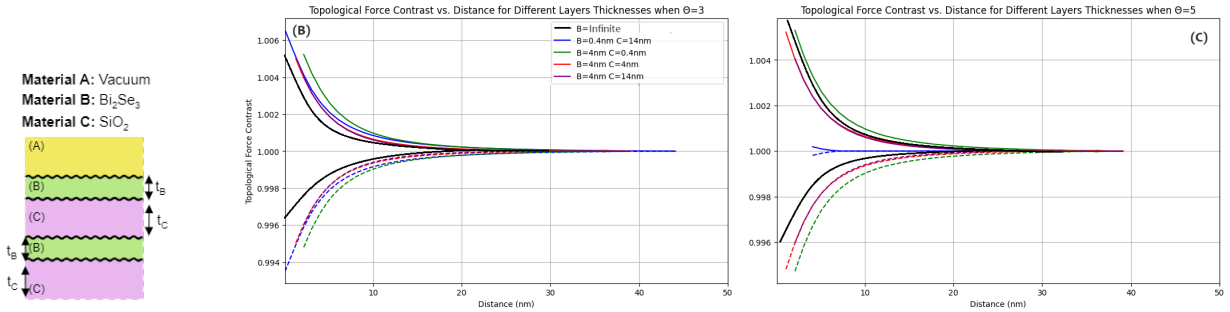

Figure 4.7: (a) Layered heterostructure composed of Vacuum (A), Bismuth Selenide (B), and Silicon Oxide (C), where repetition N=2. Layer thicknesses are denoted as t_B and surface conductivity is present. (b) Topological Force Contrast as a Function of Distance for Various Thicknesses combinations of Layer B and C for a three-layer system with repetition N=2, when θ=3 (B) or θ=5 (C).

A notable observation from the figure above is that the TFC value has decreased from 1.01 in the infinite case to 1.006 in the current scenario. Furthermore, for $\theta = 3$, the curves show smaller deviations from the baseline of 1.000 compared to those for $\theta = 5$. The curves for $\theta = 5$ display more pronounced deviations both above and below the baseline of 1.000, indicating a stronger response in topological force contrast.

In the $\theta = 3$ graph, the curves for B=0.4nm C=14nm, B=4nm C=0.4nm, B=4nm C=4nm, and B=4nm C=14nm are all above the limit case of B=Infinite, indicating more subtle changes in topological force contrast with distance.

In the $\theta = 5$ graph, the curves for the same parameters show similar variations except for the B=0.4nm C=14nm line, which is significantly smaller than in the previous case. Additionally, only the B=4nm C=0.4nm curve presents a higher topological force contrast compared to the limit case.

4.3.4 Reduction Factor for θ=5, θ=3

Figure 4.8 illustrates the reduction factor across different thickness combinations.

In the parallel case, the reduction factor curves are almost indistinguishable, irrespective of the thickness combinations of layers B and C. The reduction factor starts from 0 and increases slightly with distance, stabilizing at a low value.

The minimal variation among the curves indicates that the reduction factor in the parallel case is largely independent of the thicknesses of layers B and C. This suggests that the parallel configuration minimizes the impact of layer thickness variations on the reduction factor, resulting in no significant enhancement. In contrast, the antiparallel case shows more significant variations in the reduction factor with different thickness combinations of layers B and C. The reduction factor is higher for combinations with smaller overall thicknesses, indicating a stronger dependency on layer thickness in the antiparallel configuration.

Specifically, the curves for combinations like B=0.4nm C=0.4nm and B=0.4nm C=4nm show the

highest reduction factors, while the thicker combinations exhibit lower values. However, as all the lines are included in the limiting case, no enhancement is present.

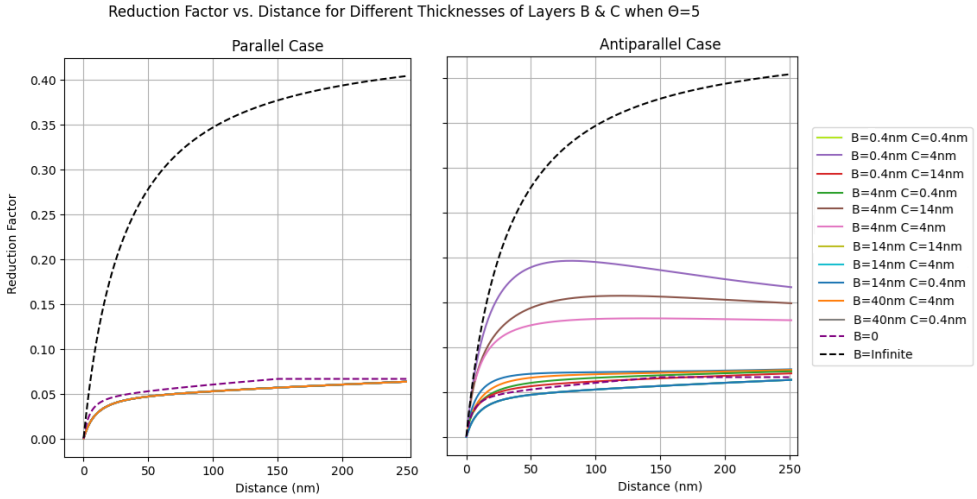

Figure 4.8: Reduction factor for different thicknesses combinations of layers B and C in both parallel and antiparallel cases.

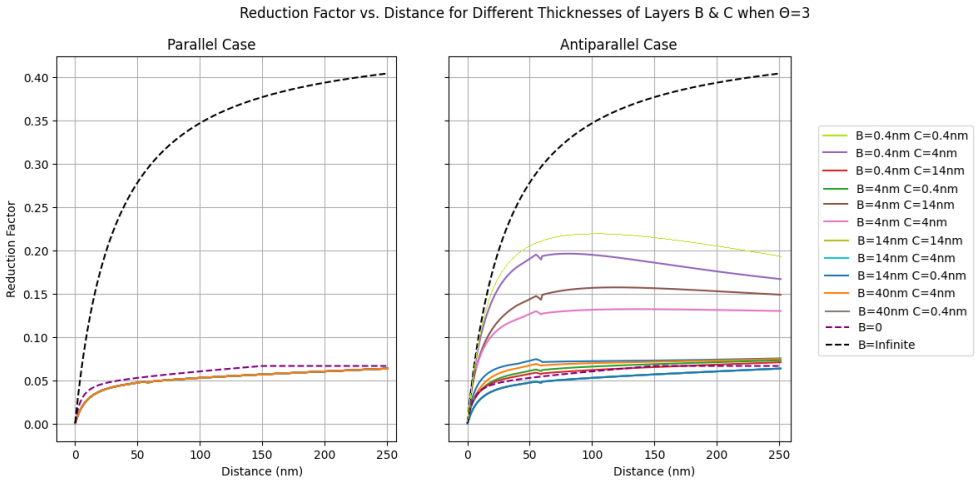

Figure 4.9: Reduction factor for different thicknesses combinations of layers B and C in both parallel and antiparallel cases.

A similar behaviour can be seen when $\theta = 3$; in this case, however, for the antiparallel case, the highest reduction factor can be seen for the smallest combination possible (B=0.4nm, C=0.4nm). It can therefore be concluded that the reduction factor does not depend significantly on the different thicknesses of layers B and C. The overall effect is minimal, showing no enhancement due to layer thickness variations.

On the contrary, the reduction factor is more sensitive to the thickness combinations of layers B and C. Smaller overall thicknesses correspond to higher reduction factor values, indicating that thinner layers enhance the reduction factor in the antiparallel configuration.

4.3.5 Comparison with Toy Model

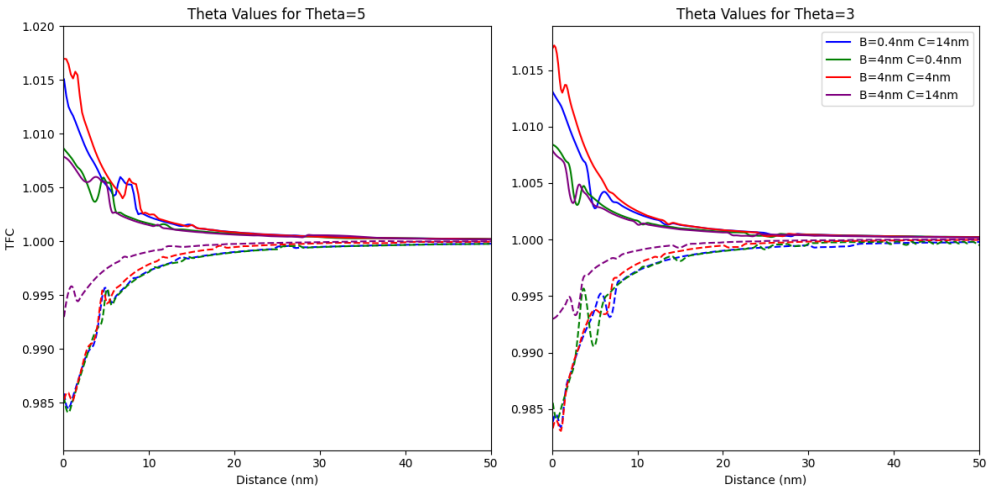

Figure 4.10: Topological Force Contrast as a Function of Distance for Various Thicknesses combinations of Layer B and C for a three-layer system with repetition N=2, when $\theta = 3$ or $\theta = 5$.

Comparing Figure 4.7 with Figure 4.10, similar trends can be observed. The initial values for the lines in the second set of graphs slightly differ from the first set but follow the same general trends. For example, the red line (B=4nm, C=14nm) shows only a 0.2% difference in TFC. The primary difference is that in the Toy model, for longer distance ranges up to 25 nm, the TFC value remains different from the limiting value of 1. This consistency indicates that the topological force contrast behaves similarly across different modelling approaches or experimental setups despite slight differences in initial values and rates of decline. Notably, in both cases of the Toy model, no enhancement is present.

Furthermore, the toy model, differently from the Bi_2Se_3 case, presents no differences in reduction factor, depending on the thickness of layer C, as shown in Figure 4.11

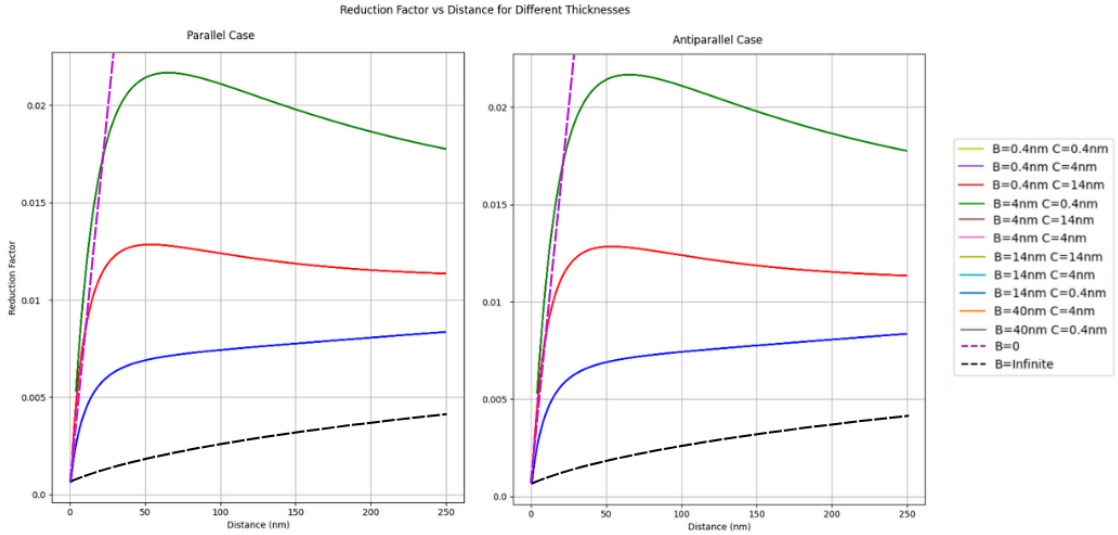

Figure 4.11: Toy Model reduction factor for different combinations of thicknesses.

Chapter 5

Conclusion

This thesis thoroughly investigated the Casimir force in multilayer systems and liquid gaps, aiming to identify configurations that enhance this force and achieve stable repulsion. Key results from the study are highlighted below:

Multilayer Systems

- The study revealed that thinner layers in multilayer systems exhibit a higher reduction factor, especially in the antiparallel configuration. This indicates that thinner layers enhance the reduction factor, making them more effective in manipulating the Casimir force.

- Comparative analysis with toy models demonstrated consistent trends across different configurations, reinforcing the non-validity of the toy model as a representation of real material phenomena. The toy model showed a significant reduction in force, particularly at shorter distances.

Topological Insulators

- Introducing surface conductivity to the top and bottom surfaces of the middle layer in a three-layer system significantly impacted the Casimir force. This effect was more pronounced in systems with topological insulators like Bi_2Se_3, where thickness and surface conductivity variations altered the electromagnetic properties and, consequently, the Casimir force.

- For both positive and negative Theta values, variations in thickness notably influenced the Topological Force Contrast (TFC) only between specific thickness pairs.

Liquid Gaps

- The analysis of the Casimir effect in liquid gaps showed that Glycerol exhibited the most significant range of TFC values compared to Methanol and Water, indicating that the properties of Glycerol greatly influence TFC variations. Water displayed a sharper initial divergence, emphasizing a more pronounced response at the onset of the interaction.

- Statistical analyses, including t-tests and ANOVA, confirmed significant differences in TFC values among the liquids. For example, the t-test comparing TFC data between Glycerol and Methanol revealed a statistically significant difference, whereas comparisons between Water and Methanol showed no significant difference.

In only one case, a significant enhancement of the Casimir force was observed as reported in Figure 4.3. However, this was due to geometrical configuration rather than the topological response of the material.

5.1 Practical Applications and Future Directions

The insights gained from the systematic exploration of Casimir force interactions in multilayer systems hold significant promise for practical applications and future research directions.

5.1.1 Practical Applications

The understanding of Casimir force dynamics in multilayer structures can be leveraged in the design and optimization of nanoscale devices and systems. For instance, the ability to control and manipulate the Casimir force through variations in layer thickness and surface properties opens up possibilities for the development of novel nanomechanical systems, such as nanoscale actuators, switches, and sensors. In addition, the possibility of achieving a stable repulsive force can help the design, fabrication, and characterization of optical materials capable of regulating the intensity and nature of the Casimir-Lifshitz force. The aim is to enable the observation and characterization of levitation phenomena resulting from the equilibrium between this force and gravity. This innovative approach relies on optical spectroscopic techniques, leveraging optical interferometry between the partially reflected and transmitted light at the interfaces of the plane-parallel system. These techniques facilitate the determination of the equilibrium distance at which the system levitates over a substrate. Recent findings from our research group suggest that certain materials possess optical constants and densities conducive to levitation when immersed in a fluid.
These self-supporting thin films, whether in single layers or multilayer configurations, must meet stringent criteria: compactness, mechanical stability, smooth surfaces, controlled thicknesses, and chemical compatibility with the surrounding fluid. The macroscopic observation of repulsive

Casimir-Lifshitz forces, facilitated by optical spectroscopic measurements, would mark an unprecedented achievement in studying fundamental matter interactions. Furthermore, the insights gained from this research can inform the development of innovative materials and coatings with tailored Casimir force properties.

5.1.2 Future Directions

Future research directions in this field could focus on two key areas:

- **Advanced Modeling Techniques:** Further refinement of computational models and simulation techniques can provide deeper insights into the complex interplay of Casimir forces in multilayer systems, for example, using more repetitions or different materials rather than SiO_2 as substrate and Bi_2Se_3 as TI.
- **Experimental Validation:** Experimental validation of theoretical predictions is crucial for verifying the accuracy and reliability of Casimir force calculations in real-world scenarios. Future research efforts should prioritize experimental studies that validate theoretical findings and explore the feasibility of practical applications.

In conclusion, this thesis investigated the effect of the Casimir force in multilayer systems and liquid gaps, seeking configurations that enhance this force. The study also compared real material data with methods that appeared to facilitate repulsion.

Appendix A

Quantum Harmonic Oscillator

An intriguing similarity emerges between the equations governing a harmonic oscillator and those describing an electromagnetic field oscillating at the same frequency. The quantization of the electromagnetic field is rooted in the quantum analysis of a harmonic oscillator. Starting with the classical Hamiltonian for a harmonic oscillator, given by $H = \frac{p^2}{2m} + \frac{m}{2}\omega^2 q^2$, a transformation of momentum and position facilitates a more convenient representation, leading to $H = \frac{\omega}{2}\left(P^2 + Q^2\right)$. This form proves advantageous for introducing complex coordinates and subsequent factorization [44].

The transformation involves redefining variables as follows:

$$H = \frac{1}{\sqrt{2}}(Q + iP) * \frac{1}{\sqrt{2}}(Q - iP) \tag{A.1}$$

Transitioning into the realm of quantum mechanics, it is well-established that the Hamiltonian of the oscillator retains a structure akin to its classical counterpart. In terms of operators:

$$\hat{H} = \frac{\omega}{2}\left(\hat{P}^2 + \hat{Q}^2\right) \tag{A.2}$$

where the operators $\hat{P}$ and $\hat{Q}$ have dimensions of $\sqrt{\hbar}$.

In the position representation, the Hamiltonian is expressed as:

$$\hat{H} = \frac{\omega}{2}\left(-\hbar^2\frac{d^2}{dQ^2} + Q^2\right) \tag{A.3}$$

with corresponding position and momentum operators:

$$\hat{Q}\psi(x,t) = x\psi(x,t), \quad \hat{P}\psi(x,t) = -i\hbar\frac{\partial}{\partial x}\psi(x,t) \tag{A.4}$$

The solutions are given by eigenfunctions $\psi_n(x)$:

$$\psi_n(x,t) = e^{-i\frac{E_n t}{\hbar}}\psi_n(x) \tag{A.5}$$

with eigenvalues:

$$E_n = \hbar\omega\left(n + \frac{1}{2}\right) \tag{A.6}$$

In the momentum representation, the position and momentum operators are interchanged [45]:

$$\hat{P}\psi(p,t) = p\psi(p,t), \quad \hat{Q}\psi(p,t) = i\hbar\frac{\partial}{\partial p}\psi(p,t) \tag{A.7}$$

The eigenvectors of the Hamiltonian are given by:

$$\psi_n(p) = \left(\frac{1}{2\pi p_c^2}\right)^{\frac{1}{4}} \frac{1}{\sqrt{2^{n!}}} e^{-\frac{p^2}{4p_c^2}} H_n\left(\frac{p}{\sqrt{2}p_c}\right) \tag{A.8}$$

where H_n represents Hermite polynomials and p_c is the characteristic momentum.

In the quantum mechanical treatment of harmonic oscillators, a pivotal aspect is the introduction of creation and annihilation operators in the energy representation. These operators, denoted as $\hat{a}$ and $\hat{a^\dagger}$, respectively, are defined in terms of position ($\hat{Q}$) and momentum ($\hat{P}$) operators:

$$\hat{a} = \frac{1}{\sqrt{2\hbar}}(\hat{Q} + i\hat{P}), \quad \hat{a^\dagger} = \frac{1}{\sqrt{2\hbar}}(\hat{Q} - i\hat{P}) \tag{A.9}$$

The Hilbert space associated with the harmonic oscillator system is spanned by a basis defined by these operators. Within this basis, the Hamiltonian ($\hat{H}$) and the number operator ($\hat{N}$) play crucial roles[46]. The Hamiltonian, representing the total energy of the system, is expressed as a function of the number operator, which counts the number of excitations in the system:

$$\hat{H} = \hbar\omega\left(\hat{a}\hat{a}^\dagger - \frac{1}{2}I\right) = \hbar\omega\left(\hat{N} + \frac{1}{2}I\right) \tag{A.10}$$

where $\hbar$ is the reduced Planck constant, ω is the angular frequency of the oscillator, and I is the identity operator.

Moreover, the commutation relations between these operators are fundamental, dictating the algebraic structure of the system [46]:

$$[\hat{N}, \hat{a}] = -\hat{a}, \quad [\hat{N}, \hat{a^\dagger}] = \hat{a^\dagger}, \quad [\hat{a}, \hat{a^\dagger}] = I \tag{A.11}$$

Operating within this basis, the creation and annihilation operators act to transition the system between different energy states. Their actions on the basis states reveal the underlying structure of the harmonic oscillator system, allowing for the determination of eigenstates and eigenvalues of the Hamiltonian.

The eigenstates, often referred to as number states or Fock states, represent distinct energy levels of the harmonic oscillator [47]:

$$|\psi_n\rangle = \frac{(\hat{a^\dagger})^n}{\sqrt{n!}}|\psi_0\rangle \tag{A.12}$$

where n is a non-negative integer representing the number of excitations, and $|\psi_0\rangle$ is the vacuum state characterized by $\hat{a}|0\rangle = 0$. These states form a complete orthonormal basis for the Hilbert space associated with the oscillator [48].

Ultimately, this formalism provides a powerful framework for understanding the quantum behavior of harmonic oscillators. Through the manipulation of creation and annihilation operators within the energy representation, one can analyze the dynamics, energy levels, and transitions of these fundamental systems with remarkable precision and insight.

Relating this to the Casimir force, the expression for the energy levels $E_n = \hbar\omega\left(n + \frac{1}{2}\right)$ highlights the zero-point energy, which is the energy of the vacuum state (n=0). The Casimir force, which arises between two conducting plates, results from these vacuum fluctuations and the zero-point energy of the quantum fields between the plates. The discrete energy levels and the role of the vacuum state are crucial in understanding how the electromagnetic field behaves in the space between the plates. The Casimir effect can be seen as a macroscopic manifestation of the principles governing quantum harmonic oscillators, where the quantum fluctuations lead to an observable attractive force. This underscores the importance of the quantum harmonic oscillator in explaining fundamental quantum phenomena such as the Casimir effect.

Appendix B

Rotation from Real Frequencies (ω) to Matsubara Frequencies (ξ_m) at $T \neq 0\,\mathrm{K}$

First, consider a system at $T = 0\,\mathrm{K}$. Rapid oscillations in the integrand of Equation (**??**) for $T = 0\,\mathrm{K}$ complicate the computation of F_{C-L}. To circumvent this, a closed integral in the complex plane can be performed. By doing so, available frequencies are now expressed as a complex variable $\Omega = \omega + i\xi$, where ω and ξ are the real and imaginary parts, respectively.

According to Cauchy's theorem, the closed integral $(\oint)$ of any function $f(\Omega)$ analytic in a region of the complex plane, such as the first quadrant of the Ω complex plane, satisfies:

$$\oint_C d\Omega\, f(\Omega) = 0 \tag{B.1}$$

where C is an arbitrary closed path within that region. In Figure 2.2(a), the closed path C consists of three segments: two straight and one circular, denoted as L_1, C_R, and L_2. Specifically, L_1 corresponds to a segment along the positive real axis $(0, \infty)$, C_R is the 90° arc with infinite radius from the positive real axis to the positive imaginary axis, and L_2 runs along the positive imaginary axis $(i\infty, 0)$. In panel (b) for $T > 0\,\mathrm{K}$, the closed path changes slightly due to poles introduced by the integrand on the ξ-axis.

If $f(\Omega)$ vanishes on the arc and is real for $f(i\xi)$, then:

$$\mathrm{Im} \int_0^\infty d\omega\, f(\omega) = \int_0^\infty d\xi\, f(i\xi) \tag{B.2}$$

It follows that:

$$F_{C-L}(d_0) = -\frac{\hbar}{2\pi^2} \int_0^\infty k_\perp dk_\perp \int_0^\infty d\xi\, k_0 \sum_{j=TE,TM} \left[\frac{e^{2k_0 d_0}}{r_j^{(0,1)}(i\xi, k_\perp) \cdot r_j^{(0,-1)}(i\xi, k_\perp)} - 1 \right]^{-1} \tag{B.3}$$

with k_l expressed in terms of $i\xi$ and $k_\perp$:

$$k_l = k_l(i\xi, k_\perp) = \left[k_\perp^2 + \varepsilon_l(i\xi)\frac{\xi^2}{c^2}\right]^{1/2} \tag{B.4}$$

and:

$$\varepsilon_l(i\xi) = 1 + \frac{2}{\pi}\int_0^\infty \frac{\omega\varepsilon_l''(\omega)}{\omega^2 + \xi^2}\, d\omega \tag{B.5}$$

In these equations, $\varepsilon_l(i\xi)$ is real for any $i\xi$ value, and $k_l(i\xi, k_\perp)$ is real for any $i\xi$ and $k_\perp$ values in Equation (B.3), eliminating complex exponentials and rapid oscillations. It is important to note that dielectric functions must be known over a wide frequency range, typically including main absorption bands, to approximate the integrated dielectric function accurately.

The Fresnel coefficients $r_j^{(0,\pm1)}$ in Equation (B.3) are expressed in terms of $i\xi$ and k

p as follows:

$$r_{TM}^{(0,\pm1)}(i\xi, k_\perp) = \frac{\varepsilon_{\pm1}(i\xi)k_0(i\xi, k_\perp) - \varepsilon_0(i\xi)k_{\pm1}(i\xi, k_\perp)}{\varepsilon_{\pm1}(i\xi)k_0(i\xi, k_\perp) + \varepsilon_0(i\xi)k_{\pm1}(i\xi, k_\perp)} \tag{B.6}$$

$$r_{TE}^{(0,\pm1)}(i\xi, k_\perp) = \frac{k_0(i\xi, k_\perp) - k_{\pm1}(i\xi, k_\perp)}{k_0(i\xi, k_\perp) + k_{\pm1}(i\xi, k_\perp)} \tag{B.7}$$

These expressions for F_{C-L} are valid for $T = 0\,\mathrm{K}$, where the only contribution to EM field fluctuations is from zero-point energy. At finite temperatures $T > 0\,\mathrm{K}$, thermal fluctuations also contribute to the Casimir-Lifshitz force.

According to Bose-Einstein statistics, the population of an EM field mode of frequency ω at finite temperature T is:

$$p(\omega) = \frac{1}{2} + \frac{1}{e^{\hbar\omega/k_BT} - 1} = \frac{1}{2}\coth\left(\frac{\hbar\omega}{2k_BT}\right) \tag{B.8}$$

The Casimir-Lifshitz force at finite temperature in real frequencies is:

$$F_{C-L}(d_0, T) = -\frac{\hbar}{2\pi^2}\int_0^\infty k_\perp dk_\perp \int_0^\infty d\omega\, \coth\left(\frac{\hbar\omega}{2k_BT}\right) \operatorname{Im}\left\{k_0 \sum_{j=TE,TM}\left[\frac{e^{2k_0d_0}}{r_j^{(0,1)}(\omega, k_\perp)\cdot r_j^{(0,-1)}(\omega, k_\perp)} - 1\right]^{-1}\right\} \tag{B.9}$$

The integral can be replaced by a summation over Matsubara frequencies $i\xi_m$:

$$\xi_m = \frac{2\pi k_BT}{\hbar}\cdot m \tag{B.10}$$

where $m = 0, 1, 2, ...$ The integral in Equation (B.9) is replaced by a summation over Mat-

subara frequencies, leading to:

$$\frac{\hbar}{2\pi}\int_0^\infty d\xi \longleftrightarrow k_B T \sum_{m'=0}^{\infty} \tag{B.11}$$

where the prime (') indicates that the term with $m = 0$ is multiplied by $1/2$. This substitution yields the expression for F_{C-L} at $T > 0\,\mathrm{K}$:

$$F_{C-L}(d_0, T) = -\frac{k_B T}{\pi}\sum_{m=0}^{\infty}\int_0^\infty k_0^m k_\perp dk_\perp$$
$$\sum_{j=TE,TM}\left[\frac{e^{2k_0^m d_0}}{r_j^{(0,1)}(i\xi_m, k_\perp)\cdot r_j^{(0,-1)}(i\xi_m, k_\perp)} - 1\right]^{-1} \tag{B.12}$$

with

$$k_l^m = k_l(i\xi_m, k_\perp) = \left[k_\perp^2 + \varepsilon_l(i\xi_m)\frac{\xi_m^2}{c^2}\right]^{1/2} \tag{B.13}$$

In these expressions, the Fresnel coefficients $r_j^{(0,1)}(i\xi_m, k_\perp)$ and $r_j^{(0,-1)}(i\xi_m, k_\perp)$ evaluated at $i\xi_m$ are given by Equations (B.6) and (B.7), respectively.

Appendix C

Casimir Energy in Infinite Plates

Let's assume we make the surface area of the two conducting plates infinite while keeping the distance *a* unchanged. This implies that the longitudinal term in the summation will be replaced by an integral (as the oscillation modes become infinite) [49].

$$\begin{aligned} E_0(a) &= \frac{\hbar}{2}\sum_J \omega_J \\ &= \frac{\hbar}{2}\sum_J |\mathbf{k}_J| \\ &= \frac{\hbar}{2}\int L^2 \frac{d^2k_\parallel}{(2\pi)^2}\left[\left|\mathbf{k}_\parallel\right| + 2\sum_{n=1}^{\infty}\sqrt{\left|\mathbf{k}_\parallel\right|^2 + \frac{n^2\pi^2}{a^2}}\right] \end{aligned} \tag{C.1}$$

This expression gives a divergent contribution. The term $(2\pi)^2$ arises from complex analysis, using the following relation:

$$\sum_{i=1}^{+\infty} f(x_i) = \frac{1}{2\pi i}\int_C f(x)\frac{d}{dx}\log F(x)dx \tag{C.2}$$

Recall that any analytic function in the entire complex plane can be represented in the following way:

$$f(z) = z^m e^{g(z)}\prod_{n=1}^{\infty}\left(1-\frac{z}{a_n}\right)e^{\frac{z}{a_n}+\frac{1}{2}\left(\frac{z}{a_n}\right)^2+\cdots+\frac{1}{m}\left(\frac{z}{a_n}\right)^{m_n}} \tag{C.3}$$

where a_n are the zeros of the function such that $\lim_{n\to\infty} a_n = 0, g(z)$ is an integral function, and m_n are integer values [50]. A corollary of the previous theorem ensures that any meromorphic function throughout the entire complex plane can be written as the ratio of two integral functions. From here, we can introduce the canonical product [31]:

$$\prod_{n=1}^{\infty}\left(1-\frac{z}{a_n}\right)e^{\frac{z}{a_n}+\frac{1}{2}\left(\frac{z}{a_n}\right)^2+\cdots+\frac{1}{h}\left(\frac{z}{a_n}\right)^h} \tag{C.4}$$

It represents an integral function and converges if the condition [51]:

$$\sum_{n=1}^{\infty} \frac{(R/|a_n|)^{h+1}}{h+1} \tag{C.5}$$

converges for any R of a uniform closed disk $|z| \leq R$. The function $\sin \pi z$ can be expressed as:

$$\sin \pi z = \pi z \prod_{n \neq 0} \left(1 - \frac{z}{n}\right) e^{\frac{z}{n}} \tag{C.6}$$

Applying the logarithmic derivative to both sides of equation, we get:

$$\pi \cot \pi z = \frac{1}{z} + \sum_{n \neq 0} \left(\frac{1}{z-n} + \frac{1}{n}\right) \tag{C.7}$$

From here, using the second integral theorem of Cauchy, for which [51]:

$$f(\xi) = \frac{1}{2\pi i} \oint_{+FD} \frac{f(z)dz}{z-\xi} \tag{C.8}$$

we represent $\frac{1}{z-\xi}$ inside as the logarithmic derivative of a function $g(z)$, represented using canonical products. Applying these considerations to our case, considering a one-dimensional case, we introduce the analytic function $F(x)$ and use a path C counterclockwise that contains the poles related to $F(x_j) = 0$.
Assuming an electromagnetic field confined in a one-dimensional box and choosing our $F(z)$ by applying periodic boundary conditions:

$$F(k) = \sin kL \tag{C.9}$$

where $k = \frac{n\pi}{L}$, with L as the side of the box. It follows [52]:

$$\begin{aligned} &= \lim_{L \to \infty} \frac{L}{2\pi} \int_{-\infty}^{+\infty} f(k) \coth(kL) dk \\ &= \frac{L}{2\pi} \int_{-\infty}^{+\infty} f(k) dk \end{aligned} \tag{C.10}$$

In N dimensions, the factorization involves the appearance of a term $(2\pi)^N$ in the denominator. The expression can be regularized in different ways. In his original article, Casimir used a frequency-damping function in which a parameter δ appears, which can be removed by taking the limit as $\delta \to 0$ [4].
Now let's consider the expression for the vacuum energy in the case where the distance a between the two conductors becomes infinite, i.e., the contribution of free energy obtained in the same

volume, a quantity that will then be subtracted from the initial energy.

$$\begin{aligned} E_0(\infty) &= \frac{\hbar}{2}\int \frac{L^2 d^2 k_\parallel}{(2\pi)^2}\int_{-\infty}^{+\infty}\frac{a dk_z}{2\pi} 2\sqrt{\left|\mathbf{k}_\parallel\right|^2 + k_z^2} \\ &= \frac{\hbar}{2}\int \frac{L^2 d^2 k_\parallel}{(2\pi)^2}\int_0^{\infty} dy \sqrt{\left|\mathbf{k}_\parallel\right|^2 + \frac{y^2\pi^2}{a^2}} \end{aligned} \tag{C.11}$$

where, in the last step, we performed the variable change $k_z = \frac{y\pi}{a}$, $dk_z = dy\frac{\pi}{a}$.

Next, we evaluate the integral over $k_\parallel$, using the representation:

$$\frac{1}{\sqrt{a^2+b^2}} = \frac{a}{b}\int_0^{\infty} e^{-t\sqrt{a^2+b^2}}dt \tag{C.12}$$

Choosing $a = \left|\mathbf{k}_\parallel\right|, b = \frac{\pi y}{a}$, the result is:

$$\begin{aligned} E_0(\infty) &= \frac{\hbar}{2}\int_0^{\infty} dy \int \frac{L^2 d^2 k_\parallel}{(2\pi)^2}\frac{\pi y}{a} e^{-y\sqrt{\left|\mathbf{k}_\parallel\right|^2 + \frac{\pi^2 y^2}{a^2}}} \\ &= \frac{\hbar}{2}\int_0^{\infty} dy \frac{\pi y}{a} e^{-y\pi/a}\int \frac{L^2 d^2 k_\parallel}{(2\pi)^2} e^{-y\sqrt{\left|\mathbf{k}_\parallel\right|^2}} \end{aligned} \tag{C.13}$$

Now, we evaluate the integral over $k_\parallel$:

$$\begin{aligned} &= \frac{\hbar}{2}\int_0^{\infty} dy \frac{\pi y}{a} e^{-y\pi/a}\frac{L^2}{2\pi}\int_{-\infty}^{+\infty} dk_x \int_{-\infty}^{+\infty} dk_y e^{-y\sqrt{\left|\mathbf{k}_\parallel\right|^2}} \\ &= \frac{\hbar L^2}{4a}\int_0^{\infty} dy y e^{-y\pi/a}\int_{-\infty}^{+\infty} dk_x \int_{-\infty}^{+\infty} dk_y e^{-y\sqrt{k_x^2+k_y^2}} \\ &= \frac{\hbar L^2}{4a}\int_0^{\infty} dy y e^{-y\pi/a}\pi \end{aligned} \tag{C.14}$$

The integral over k_x and k_y is calculated using polar coordinates [51], and the final result is:

$$E_0(\infty) = \frac{\hbar\pi^2}{8a^2}L^2 \tag{C.15}$$

The Casimir energy, defined as the difference between the vacuum energy in the finite and infinite cases, is then [53]:

$$\begin{aligned} \Delta E &= E_0(a) - E_0(\infty) \\ &= \frac{\hbar}{2}\int \frac{L^2 d^2 k_\parallel}{(2\pi)^2}\sum_{n=1}^{\infty} 2\sqrt{\left|\mathbf{k}_\parallel\right|^2 + \frac{n^2\pi^2}{a^2}} \\ &- \frac{\hbar\pi^2}{8a^2}L^2 \end{aligned} \tag{C.16}$$

Introducing cylindrical coordinates $\left|\mathbf{k}_\parallel\right| = \rho\cos\theta, n\pi/a = \rho\sin\theta$ and performing the integration over θ, the Casimir energy becomes:

$$\Delta E = \frac{\hbar}{4\pi}\int_0^\infty d\rho\rho\left[\sqrt{\rho^2+\frac{\pi^2}{a^2}}+\sqrt{\rho^2+\frac{4\pi^2}{a^2}}+\sqrt{\rho^2+\frac{9\pi^2}{a^2}}+...\right] \tag{C.17}$$

The sum of square roots can be expressed in terms of the Riemann zeta function:

$$\sum_{n=1}^{\infty}\sqrt{\rho^2+\frac{n^2\pi^2}{a^2}} = \frac{1}{\pi a}\sum_{n=1}^{\infty}K_0\left(\frac{2\pi n\rho}{a}\right) \tag{C.18}$$

where K_0 is the modified Bessel function of the second kind.
The Casimir energy can then be written as:

$$\Delta E = \frac{\hbar}{4\pi a}\int_0^\infty d\rho\rho K_0\left(\frac{2\pi\rho}{a}\right) \tag{C.19}$$

The integral above is divergent, and a regularization procedure is needed. One common method is to use zeta function regularization, where the Riemann zeta function is employed to give meaning to series [51].

$$E^* = \frac{\hbar\pi^2}{a^3}B_4 4! \tag{C.20}$$

where $B_4 = -\frac{1}{30}$ therefore this technique yields the following expression for the Casimir energy [28].:

$$\Delta E = -\frac{\pi^2\hbar c}{720a^3} \tag{C.21}$$

Appendix D

Measurements of Casimir Force

In this chapter, we will discuss the basics of experiments conducted to measure the Casimir force, keeping in mind that it becomes measurable at a distance of $\sim 1\mu m$ and is on the order of 10^{-7}N for a surface area of $1\ \mathrm{cm}^2$. The first experiment on the Casimir force was performed by Sparnay, who reported a 100% error [54].

D.1 Experimental Basis for Measurement

The technical prerequisites for Casimir force measurement demand precise surface separation and high instrument sensitivity [54]. Sparnay emphasized the need for chemically clean, flat surfaces and accurate distance measurements, while minimizing potential differences to mitigate electrostatic forces [55]. However, practical challenges arise, such as impurities on glass or quartz surfaces altering force measurements [56]. Notably, recent experiments by Sparnay, van Blokland, and Overbeek explored metal surfaces, followed by Lamoreaux's torsion pendulum and Mohideen's atomic force microscopy approaches [54]–[56].

D.2 Sparnay's Experiment, 1958

Sparnay's experiment [1] provided the first indication of an attractive Casimir force between two metallic surfaces, although conclusive information was not obtained. He tried to measure the force using a dynamometer with a sensitivity of $(0.1 - 1) \times 10^{-3} dyn$.
The capacitance of the system consisting of the two metal plates (from which the required extension to the spring was derived) was calibrated using tungsten and platinum wires.
The entire apparatus was isolated from vibrations, and the metal surfaces were electrically isolated from the rest of the instrumentation and the environment. The use of the spring led to significant difficulties in evaluating the distance between the surfaces.

[1] Information in this section have been sourced from [9]

Sparnay also found that a potential difference between the media of $17\mathrm{mV}$ was sufficient to make force measurement impossible. For this reason, at the beginning of the experiment, the two plates were brought into contact.
Three sets of surfaces were used for measurements, namely aluminum-aluminum, chromium-chromium, and chromium-steel, trying to achieve maximum alignment for each set. It was also taken into account that, due to the presence of residual particles on the surfaces, the distance between the two plates in "contact" had to be about $0.2\mu m$. Repulsive forces were measured in the aluminum-aluminum set, and Sparnay believed that to eliminate them from the measurements, it was necessary to improve the instrumental settings of the experiment, requiring greater accuracy for both the measurement of the distance between the two planes and their parallelism, as well as for the presence of potential differences due to residual particles on metals. In the case of the chromium-chromium and chromium-steel sets, an attractive force measurement was obtained, but the uncertainty in the measurements was too significant for a meaningful comparison with theory.

D.3 Van Blokland and Overbeek's Experiment, 1978

Van Blokland and Overbeek also used a balanced spring to measure the force between a lens (thus a curved surface) and a plate covered with a layer of 100 ± 5 nm or 50 ± 5 nm of chromium, which was then covered with a film of $1 - 2$ nm of oxide [2]. Water vapor was used to reduce charges on the surfaces. The problems encountered in this experiment included the presence of undesired potential differences between the two plates and the impossibility of obtaining a good measure of the distance between the two media, as in Sparnay's experiment. They tried to solve the first of these problems by seeking the minimum of the Casimir force as a function of an applied potential, balancing potential differences. In fact, their measurement gave a value between 19 and $20\mathrm{mV}$, an amount that for a distance of 400 nm was equal to the sought Casimir force. The presence of the chromium surface also proved problematic, as chromium has strong absorption bands for 600 nm. To experimentally reproduce the Lifshitz model, the imaginary part of the dielectric function corresponding to absorption was treated as a Lorentzian atom, and the two overlapping bands were treated as a single absorption band. The absorption force was evaluated as 40% of the total force. The uncertainty in force measurements was 25% near 150 nm, and the overall accuracy of the experiment was estimated at 50%.

D.4 Lamoreaux's Experiment, 1997

Lamoreaux's experiment [3] opened a modern phase of Casimir force measurements. His experimental setup consisted of a torsion pendulum for force measurement, a spherical lens with a radius

[2] Information in this section have been sourced from [57]
[3] Information in this section have been sourced from [58]

of 11.3 ± 0.1 cm and a flat surface. The two surfaces were covered with a layer of 0.5μm of copper, further coated with 0.5μm of gold through evaporation. The lens was mounted on a piezo, while the flat surface was attached to one arm of the torsion pendulum. The other arm of the torsion balance was connected to the center of two capacitors, so that the torsion angle could be controlled by the potential between the two capacitors. The potential difference to balance the capacitance difference was the measure of the Casimir force. Due to the application of potential from the piezo, the lens was moved, and during the experiment, measurements were divided into 16 steps, varying both distances and applied potentials related to the measurement of the torsion balance angle. The total force was measured within 10μm of distance between the surfaces.
The experiment was repeated by changing the variables at each step and reported values of the residual electrostatic force and the distance between the surfaces in contact through a fit between the expected value of the Casimir force and the measured total force.
The fit function has the following form:

$$F^m(i) = F_C^T(a_i + a_0) + \frac{\beta}{a_i + a_0} + b$$

where $F^m(i)$ is the measured total force at the i-th step, F_C^T is the theoretical Casimir force, a_0 is a fit parameter that accounts for the absolute separation of contact between the surfaces, b is a constant, and β represents the electrostatic force between the surfaces.
The relationship between the experimental measured force F_C^m and the theoretical one F_c^T was:

$$F_C^m\,(a_i) = (1 + \delta)F_c^T + b'$$

D.5 Mohideen's Experiment, 1998

Thanks to contributions and information from less recent experiments, such as Sparnay's, which highlighted the issues of his experimental setup, emphasizing, for example, the need to use non-reactive materials with as few residues as possible, Mohideen succeeded in obtaining the most significant result for the Casimir force measurement in 1998 [4]. He used atomic force microscopy (AFM) and reported a statistical precision of 1% for the measured minimum distance. His first experiment involved a system consisting of a polystyrene sphere with a diameter of $200 \pm 4\mu$m, a cantilever, photodiodes, and a laser source.

[4] Information in this section have been sourced from [58]

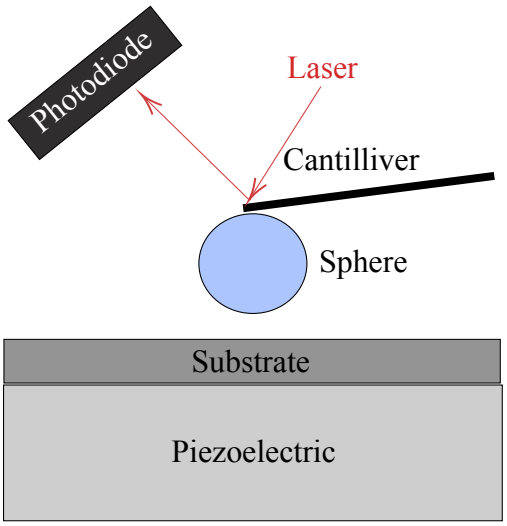

Figure D.1: Mohideen's experimental set-up.

The deflection of the cantilever beam is measured by the deflection of the laser beam, whose signal difference is collected by the photodiodes. The signal difference is calibrated by an electrostatic force. The sphere is mounted on the tip of the metallic cantilever beam, the latter covered with a layer of silver. The beam, the sphere, and the plate are in turn covered with a layer of $300\ \mathrm{nm}$ of aluminum through evaporation. The choice of aluminum is justified by the fact that it is very reflective for small wavelengths (thus allowing small distances between surfaces), and it adheres well to various metals. Also, aluminum has a low melting point. During the experiment, the plate is moved towards the sphere in steps of $3.6\ \mathrm{nm}$, and the corresponding signal reaching the photodiodes is measured. From the obtained data, it was found that for large separations between surfaces, a linear signal was measured, due to the increasing number of laser beams deflected and captured by the diodes [59]. Instead, for separations ranging from contact between surfaces to $350\ \mathrm{nm}$, the data effectively represented the attractive Casimir force.

Appendix E

The Electro-Magnetic Theory

The concept of vacuum energy resurfaces in connection with the advancement of quantum theory, particularly through the quantization of the electromagnetic field. This chapter begins by laying down the groundwork for a comprehensive examination of the quantum perspective. It explores the essential principles of classical electromagnetism, delineating Maxwell's equations, introducing electromagnetic potentials, and subsequently delving into the wave equation and gauge transformations.

E.1 Maxwell's equations

Maxwell's equations stand out for their ability to depict the phenomena of classical electrodynamics [60]. They are expressed locally as linear differential equations in four variables, incorporating the charge density $\rho(\mathbf{x}, t)$ and current density $\mathbf{j}(\mathbf{x}, t)$. These equations establish connections between various physical quantities computed at the same location [61].

$$\begin{aligned} &1)\ \nabla \cdot \mathbf{E}(\mathbf{x}, t) = 4\pi\rho(\mathbf{x}, t) \\ &2)\ \nabla \cdot \mathbf{B}(\mathbf{x}, t) = 0 \\ &3)\ \nabla \times \mathbf{E}(\mathbf{x}, t) + \frac{1}{c}\frac{\partial \mathbf{B}(\mathbf{x}, t)}{\partial t} = 0 \\ &4)\ \nabla \times \mathbf{B}(\mathbf{x}, t) - \frac{1}{c}\frac{\partial \mathbf{E}(\mathbf{x}, t)}{\partial t} = \frac{4\pi}{c}\mathbf{j}(\mathbf{x}, t). \end{aligned} \tag{E.1}$$

In particular, the first equation is a result of applying the divergence theorem and Gauss's theorem to the electric field vector, with the only requirement that the field **E** is differentiable at every point in the considered domain, an assumption not considered for the sole validity of Gauss's theorem [62].

Deriving the second equation from the fundamental law of magnetostatics (Biot and Savart) [63],

$$\mathbf{B}(\mathbf{r}) = \frac{\mu_0}{4\pi}\oint_{l'} I\frac{d\mathbf{l}' \times \Delta\mathbf{r}}{|\Delta\mathbf{r}|^3}, \tag{E.2}$$

where l' is a closed circuit and μ_0 is the vacuum magnetic permeability. Applying the divergence operator:

$$\nabla \cdot \mathbf{B} = \frac{\mu_0 I}{4\pi} \oint_{l'} \nabla \cdot \frac{d\mathbf{l}' \times \Delta\mathbf{r}}{|\Delta\mathbf{r}|^3}, \tag{E.3}$$

and using the divergence operator, we obtain [64]:

$$\nabla \cdot \mathbf{B} = \frac{\mu_0 I}{4\pi} \oint_{l'} \left[\frac{\Delta\mathbf{r}}{|\Delta\mathbf{r}|^3} \cdot (\nabla \times d\mathbf{l}') - d\mathbf{l}' \cdot \left(\nabla \times \frac{\Delta\mathbf{r}}{|\Delta\mathbf{r}|^3} \right) \right] = 0, \tag{E.4}$$

leading to the second Maxwell equation $\nabla \cdot \mathbf{B}(\mathbf{x}, t) = 0$ [65].
Repeating the same reasoning after rewriting the fundamental law of magnetostatics using the current density $\mathbf{J}(\mathbf{r}')$,

$$\mathbf{B}(\mathbf{r}) = \frac{\mu_0}{4\pi} \int_{\tau'} \frac{\mathbf{J}(\mathbf{r}^9) \times \Delta\mathbf{r}}{\Delta r^3} d\tau', \tag{E.5}$$

we obtain the fourth Maxwell equation in the stationary, vacuum case: $\nabla \times \mathbf{B} = \mu_0 \mathbf{J}$ [61].
The third equation, referred to as the Faraday-Neumann law, delineates the behavior of the electric field's motion, while the fourth equation, Ampère's law, characterizes the motion of the magnetic field. Together, these four pivotal relationships illustrate the potential for generating magnetic fields from electric fields and vice versa.
Moreover, it's noteworthy that the electric and magnetic field vectors can be broken down into both transverse and longitudinal components, as follows [66]:

$$\begin{aligned} \mathbf{E} &= \mathbf{E}_L + \mathbf{E}_T \\ \mathbf{B} &= \mathbf{B}_L + \mathbf{B}_T \end{aligned} \tag{E.6}$$

We establish that the transverse components of the fields govern the dynamics of the system. This is demonstrated by utilizing the decomposition of the electric field into components within the first Maxwell equation:

$$\nabla \cdot \mathbf{E} = \nabla \cdot (\mathbf{E}_L + \mathbf{E}_T) \tag{E.7}$$

But using Gauss's law, we have

$$\nabla \cdot \mathbf{E}_T = 0 \tag{E.8}$$

$$\nabla \cdot \mathbf{E} = \nabla \cdot \mathbf{E}_L = 4\pi\rho \tag{E.9}$$

With a similar procedure regarding the second Maxwell equation, we arrive at the conclusion that the longitudinal component of the magnetic field is solenoidal [65].

$$\nabla \cdot \mathbf{B}_L = 0 \tag{E.10}$$

Additionally, being irrotational, $B_L = 0$, implying that $B = B_T$. Consequently, the magnetic field solely possesses a transverse component. Concerning the charge density $\mathbf{j}(\mathbf{x}, t)$, it's crucial to recall its adherence to the continuity equation $\nabla \cdot \mathbf{j} + \frac{\partial \rho}{\partial t} = 0$ [60].

E.2 Electromagnetic Potentials

The vector potential of the magnetic field, denoted as $\mathbf{A}$, is a field in which the magnetic field equals its curl [60], expressed

$$\mathbf{B} = \nabla \times \mathbf{A} \tag{E.11}$$

It's worth noting that considering a vector of the form $\mathbf{A}' = \mathbf{A} + \nabla f$, where f is any scalar function, also yields a potential vector. This relationship is termed a gauge transformation.
For a vector potential with zero divergence, it suffices that $\nabla^2 f = -\nabla \cdot \mathbf{A}$ [67]. Maxwell's equations consist of six independent first-order partial differential equations relating the six components of the electric and magnetic fields. Analytical solutions are feasible only in simple cases. Utilizing equations in terms of the vector potential $\mathbf{A}$ and scalar potential V, which we'll introduce later, offers advantages by reducing the number of equations to four second-order differential equations. Moreover, this approach allows for decoupled equations, each containing only one of the unknown functions A_x, A_y, A_z, and V.
It's important to highlight that the second Maxwell equation $\nabla \cdot \mathbf{B}(\mathbf{x}, t) = 0$ holds even under non-stationary conditions. For a time-dependent magnetic field, we define the vector potential through the relation [67]:

$$\begin{aligned} \nabla \times \mathbf{A} &= \mathbf{B} \\ \mathbf{A} &= \mathbf{A}(\mathbf{r}, t) \end{aligned} \tag{E.12}$$

Now, introducing this definition into the third Maxwell equation, we find:

$$\begin{aligned} \nabla \times \mathbf{E} = -\frac{\partial \mathbf{B}}{\partial t} = -\frac{\partial}{\partial t}(\nabla \times \mathbf{A}) = -\nabla \times \left(\frac{\partial \mathbf{A}}{\partial t}\right) \\ \nabla \times \left(\mathbf{E} + \frac{\partial \mathbf{A}}{\partial t}\right) = 0 \end{aligned} \tag{E.13}$$

Since the vector $\mathbf{E} + \frac{\partial \mathbf{A}}{\partial t}$ is irrotational, it can be expressed as the gradient of a scalar potential V:

$$-\nabla V - \frac{\partial \mathbf{A}}{\partial t} = \mathbf{E} \tag{E.14}$$

By introducing potentials, the second and third Maxwell equations (which are homogeneous equations without source terms) are automatically satisfied [60]:

$$\begin{aligned} \nabla \cdot \mathbf{B} &= \nabla \cdot (\nabla \times \mathbf{A}) = 0 \\ (\nabla \times \mathbf{E}) + \frac{\partial \mathbf{B}}{\partial t} &= \nabla \times \left(\mathbf{E} + \frac{\partial \mathbf{A}}{\partial t} \right) = \nabla \times (-\nabla V) = 0 \end{aligned} \tag{E.15}$$

Consequently, for determining potentials, the non-homogeneous Maxwell equations are utilized [67]:

$$\begin{cases} \nabla^2 V + \frac{\partial}{\partial t}(\nabla \cdot \mathbf{A}) = -\frac{\rho}{\varepsilon} \\ \nabla^2 \mathbf{A} - \varepsilon\mu \frac{\partial^2 \mathbf{A}}{\partial t^2} - \nabla(\nabla \cdot \mathbf{A} + \varepsilon\mu \frac{\partial V}{\partial t}) = -\mu \mathbf{J} \end{cases} \tag{E.16}$$

assuming ε and μ are constants and uniform. However, these equations are still not decoupled. To achieve decoupled equations, we introduce the following gauge transformations:

$$\begin{cases} \mathbf{A} \to \mathbf{A}' = \mathbf{A} + \nabla\varphi \\ V \to V' = V - \frac{\partial \varphi}{\partial t} \end{cases} \tag{E.17}$$

where φ is a scalar function in the variables $\mathbf{r}$ and t called the gauge function. An appropriate choice allows us to arrive at a system of decoupled equations, and the condition for this to happen is that the potentials satisfy the Lorenz condition [60]:

$$\nabla \cdot \mathbf{A} + \varepsilon\mu \frac{\partial V}{\partial t} = 0 \tag{E.18}$$

Thus, the system of electrodynamics equations becomes:

$$\begin{cases} \nabla^2 \mathbf{A} - \varepsilon\mu \frac{\partial^2 \mathbf{A}}{\partial t^2} = -\mu \mathbf{J} \\ \nabla^2 V - \varepsilon\mu \frac{\delta^2 V}{\partial t^2} = -\frac{\rho}{\epsilon} \end{cases} \tag{E.19}$$

When the potentials satisfy the Lorenz condition, they are said to belong to the Lorenz gauge [67]. Note the formal analogy of the electrodynamics equations written in terms of potentials belonging to this gauge in the general case and the equations describing the behavior of fields in the steady-state case.

E.3 Coulomb's Gauge

Another important gauge condition is given by the Coulomb gauge, with the condition $\nabla \cdot \mathbf{A} = 0$ (i.e., the vector potential is solenoidal), leading to a Poisson equation of the form $\nabla^2 V = 4\pi\rho$. Indeed, by substituting the gauge into Equation E.21, the potentials V and $\mathbf{A}$ satisfy the following conditions [60]:

$$\begin{aligned} \nabla^2 V &= -\frac{\rho}{\varepsilon} \\ \nabla^2 \mathbf{A} - \varepsilon\mu\frac{\partial^2 \mathbf{A}}{\partial t^2} &= \varepsilon\mu\nabla\frac{\partial V}{\partial t} - \mu\mathbf{J} \end{aligned} \tag{E.20}$$

The first of these equations has a solution of the form [61]:

$$V(\mathbf{x}, t) = \int \frac{\rho\left(\mathbf{x}', t\right)}{|\mathbf{x} - \mathbf{x}'|} d^3\mathbf{x}' \tag{E.21}$$

It represents the instantaneous Coulomb potential due to the charge density. The Coulomb gauge is generally used in the absence of sources ($\rho = 0$, $\mathbf{J} = 0$) and is therefore also called the pure radiation gauge.

E.4 Electromagnetic Wave Equation

Let's rewrite the Maxwell's equations for an infinite, isotropic, and homogeneous dielectric medium, assuming the medium is everywhere electrically neutral, i.e., its ρ is $\rho = 0$ [61]:

$$\begin{aligned} 1)\nabla \cdot \mathbf{E} &= 0 \\ 2)\nabla \cdot \mathbf{B} &= 0 \\ 3)\nabla \times \mathbf{E} &= \frac{\partial \mathbf{B}}{\partial t} \\ 4)\nabla \times \mathbf{B} &= \epsilon\mu\frac{\partial \mathbf{E}}{\partial t} \end{aligned} \tag{E.22}$$

and apply the curl to the third equation [61], obtaining

$$-\nabla^2 \mathbf{E} = \nabla \times \frac{\partial \mathbf{B}}{\partial t} = -\frac{\partial}{\partial t}(\nabla \times \mathbf{B}) \tag{E.23}$$

Now, evaluating the time derivative of the fourth Maxwell equation, we arrive at the wave equation for the **E** field:

$$\nabla^2 \mathbf{E} = \epsilon\mu\frac{\partial^2 \mathbf{E}}{\partial t^2} \tag{E.24}$$

Applying the curl to the fourth equation and with a similar procedure, we obtain the electromagnetic wave equations:

$$\begin{cases} \nabla^2 \mathbf{E} = \epsilon\mu\frac{\partial^2 \mathbf{E}}{\partial t^2} \\ \nabla^2 \mathbf{B} = \epsilon\mu\frac{\partial^2 \mathbf{B}}{\partial t^2} \end{cases} \tag{E.25}$$

Their solution is represented by waves propagating at the speed $v = \frac{1}{\sqrt{\varepsilon\mu}}$ [61].
Note that the electrodynamics equations written in terms of vector potential and scalar potential, in the absence of sources, coincide with the wave equation [61]:

$$\begin{cases} \nabla^2 \mathbf{A} - \varepsilon\mu \frac{\partial^2 \mathbf{A}}{\partial t^2} = 0 \\ \nabla^2 V - \varepsilon\mu \frac{\partial^2 V}{\partial t^2} = 0 \end{cases} \tag{E.26}$$

E.5 A fluctuating vacuum

To understand the origin of the Casimir force, it is crucial to delve into the consequences of electromagnetic fluctuations and how a fluctuating electromagnetic field can result in a non-zero pressure. Examining Maxwell's stress tensor in space, denoted as [68]:

$$\sigma_{ij} = \epsilon_0 E_i E_j + \frac{1}{\mu_0} B_i B_j - \frac{1}{2}\left(\epsilon_0 E^2 + \frac{1}{\mu_0} B^2\right)\delta_{ij} \tag{E.27}$$

Here, σ_{ij} represents the i, j component of the stress tensor in rectangular coordinates ($i, j \in \{x, y, z\}$), $E_i(B_i)$ is the electric (magnetic) field in the i direction, ϵ_0 and μ_0 are the vacuum permittivity and permeability, respectively, and δ_{ij} is the Kronecker symbol [30]. Taking the expectation value of E on both sides reveals that the stress tensor is diagonal: $\sigma_{ij} = -P\delta_{ij}$, where P is given by [69]:

$$P = \frac{1}{3}\mathbb{E}\left[\frac{\epsilon_0}{2}|E|^2 + \frac{1}{2\mu_0}|B|^2\right] = \frac{1}{3}\mathbb{E}[u] \tag{E.28}$$

The expression inside the expected value corresponds to the electromagnetic energy density u. Notably, u depends quadratically on the magnitude of the fields. Consequently, a fluctuating electromagnetic field generates a non-zero pressure even when the average field is zero ($\mathbb{E}[E_i] = \mathbb{E}[B_j] = 0$, yet $P \neq 0$). This phenomenon is feasible because the second moment of any non-degenerate random variable is always nonzero, implying $\mathbb{E}[E_i^2] \neq 0 \Longrightarrow P \neq 0$ [70].

Appendix F

Derivation Liftshitz Energy

Electric and magnetic fields can be expressed in the exponential form [71]:

$$\mathbf{E}^{(i)}_{\mathbf{k}_{||}}(t,\mathbf{r}) = \mathbf{f}^{(i)}\left(\mathbf{k}_{\parallel}, z\right) e^{i(k_x x + k_y y) - i\omega t} \tag{F.1}$$

$$\mathbf{B}^{(i)}_{\mathbf{k}_{||}}(t,\mathbf{r}) = \mathbf{g}^{(i)}\left(\mathbf{k}_{\parallel}, z\right) e^{i(k_x x + k_y y) - i\omega t} \tag{F.2}$$

where the index i indicates the polarization state. The wave equations for the electric and magnetic fields ($\mu = 1$) are:

$$\nabla^2 \mathbf{E}^{(i)}_{\mathbf{k}_{||}}(t,\mathbf{r}) - \frac{\varepsilon}{c^2}\frac{\partial^2 \mathbf{E}^{(i)}_{\mathbf{k}_{||}}(t,\mathbf{r})}{\partial t^2} = 0 \tag{F.3}$$

$$\nabla^2 \mathbf{B}^{(i)}_{\mathbf{k}_{||}}(t,\mathbf{r}) - \frac{\varepsilon}{c^2}\frac{\partial^2 \mathbf{B}^{(i)}_{\mathbf{k}_{||}}(t,\mathbf{r})}{\partial t^2} = 0 \tag{F.4}$$

With respect to the z axis, we have [72] :

$$\frac{d^2 f^{(i)}}{dz^2} - R^2 f^{(i)} = 0 \tag{F.5}$$

$$\frac{d^2 g^{(i)}}{dz^2} - R^2 g^{(i)} = 0 \tag{F.6}$$

Here, we have introduced [71]:

$$R^2 = k_{\parallel}^2 - \varepsilon(\omega)\frac{\omega^2}{c^2} \tag{F.7}$$

$$k_{\parallel}^2 = k_1^2 + k_2^2 \tag{F.8}$$

The differential equation F.6 has a solution of the form [72] :

$$f_z = f_{z,1} = Ae^{Rz}, \quad \text{if} \quad z \leq 0 \tag{F.9}$$
$$f_z = f_{z,2} = Be^{R_0 z} + Ce^{-R_0 z}, \quad \text{if} \quad 0 \leq z \leq d \tag{F.10}$$
$$f_z = f_{z,3} = De^{-Rz}, \quad \text{if} \quad z \geq d \tag{F.11}$$

with

$$R = \sqrt{k_\parallel^2 - \varepsilon(\omega)\frac{\omega^2}{c^2}}, \quad R_0 = \sqrt{k_\parallel^2 - \frac{\omega^2}{c^2}} \tag{F.12}$$

We impose continuity conditions at $z = 0$ and $z = d$ for $\frac{\partial f_z}{\partial z}$ and εf_z:

$$\varepsilon f_{z,1}(0) = \varepsilon f_{z,2}(0), \qquad \varepsilon f_{z,2}(d) = \varepsilon f_{z,3}(d) \tag{F.13}$$
$$f'_{z,1}(0) = f'_{z,2}(0), \qquad f'_{z,2}(d) = f'_{z,3}(d) \tag{F.14}$$

which results in [72] :

$$\varepsilon A = \varepsilon B + \varepsilon C \tag{F.15}$$
$$\varepsilon B e^{R_0 d} + \varepsilon C e^{-R_0 d} = De^{-Rd} \tag{F.16}$$
$$RA = BR_0 - CR_0 \tag{F.17}$$
$$R_0 B e^{R_0 d} - R_0 C e^{-R_0 d} = -RDe^{-Rd} \tag{F.18}$$

Setting the discriminant of the coefficient matrix of the resulting homogeneous linear system to zero, ensuring the existence of nontrivial solutions, leads to the equation [73]:

$$D(\omega) = e^{-R_0 d}\left(\varepsilon(\omega)R_0 - R\right)^2 + e^{R_0 d}\left(\varepsilon(\omega)R_0 + R\right)^2 \tag{F.19}$$

Similarly, the boundary conditions for f_y and $\frac{df_y}{dy}$ lead to a similar result for the perpendicular polarization [73].
Using the second Cauchy's theorem [73]:

$$f(\xi) = \frac{1}{2\pi i}\oint_{+FD} \frac{f(z)dz}{z - \xi}, \tag{F.20}$$

representing $\frac{1}{z-\xi}$ inside as the logarithmic derivative of a function $g(z)$ using canonical products

[51], we use the following formula to derive the zero-point energy:

$$\frac{1}{2\pi i}\int_C z\frac{d}{dz}\ln g(z)dz \tag{F.21}$$

In our case, we will use a function of the form $g(z)=\sin\pi z$, as:

$$\sin\pi z=\pi z\prod_{n\neq 0}\left(1-\frac{z}{n}\right)e^{\frac{z}{n}}, \tag{F.22}$$

and its logarithmic derivative results in a summation of terms of the form $\frac{1}{z-\xi}$. In our discussion, the function $g(\omega_i)=D(\omega)$. Indeed, it is a function that vanishes for every ω_i in the spectrum [51].

$$\sum_J \omega_J=\frac{1}{2\pi i}\left[\int_{i\infty}^{i\infty}\omega d\ln D(\omega)+\int_{C_+}\omega d\ln D(\omega)\right] \tag{F.23}$$

Where C_+ is the upper semicircle of infinite radius in the complex plane centred at the origin. We evaluate the integral $\int_{C_+}\omega d\ln D(\omega)$ with the conditions [74]:

$$\lim_{\omega\to\infty}\varepsilon(\omega)=1 \tag{F.24}$$

$$\lim_{\omega\to\infty}\frac{d\varepsilon(\omega)}{d\omega}=0 \tag{F.25}$$

in all directions of the complex ω plane. It follows:

$$\int_{C_+}\omega d\left[\ln\left(e^{-R_0 d}\left(\varepsilon(\omega)R_0-R_1\right)^2+e^{R_0 d}\left(\varepsilon(\omega)R_0+R\right)^2\right)\right] \tag{F.26}$$

$$\int_{C_+}\omega\frac{d\left[\ln\left(e^{-R_0 d}\left(\varepsilon(\omega)R_0-R_1\right)^2+e^{R_0 D}\left(\varepsilon(\omega)R_0+R\right)^2\right)\right]}{d\omega}d\omega(2 \tag{F.27}$$

$$=\int_{C_+}\omega\frac{d[\ln D(\omega)]}{d\omega}d\omega \tag{F.28}$$

And by performing the $\lim_{\omega\to\infty}\frac{d[\ln D\omega)]}{d\omega}$, taking into account all dependencies on ω in R and R_0 in the derivative calculation, it follows [74]:

$$\int_{C_+}\omega d\ln D(\omega)=4\int_{C_+}d\omega \tag{F.29}$$

Introducing a new variable $\zeta = -i\omega$:

$$\sum_J \omega_J = \frac{1}{2\pi}\int_{\infty}^{-\infty} \zeta d\ln D(i\zeta) + \frac{2}{\pi}\int_{C_+} d\zeta \tag{F.30}$$

We take the $\lim_{d\to\infty} D(\omega)$:

$$\lim_{d\to\infty}\sum_J \omega_J = \frac{1}{2\pi}\int_{\infty}^{-\infty} \zeta d\ln D_\infty(i\zeta) + \frac{2}{\pi}\int_{C_+} d\zeta \tag{F.31}$$

$$\lim_{d\to\infty} D = D_\infty \tag{F.32}$$

$$\left(\sum_J \omega_J\right)_{ren} = \tag{F.33}$$

$$= \sum_J \omega_J - \lim_{d\to\infty}\sum_J \omega_J \tag{F.34}$$

$$= \frac{1}{2\pi}\int_{\infty}^{-\infty} \zeta d\ln D(i\zeta) + \frac{2}{\pi}\int_{C_+} d\zeta \tag{F.35}$$

$$- \frac{1}{2\pi}\int_{\infty}^{-\infty} \zeta d\ln D_\infty(i\zeta) - \frac{2}{\pi}\int_{C_+} d\zeta \tag{F.36}$$

$$\left(\sum_J \omega_J\right)_{ren} = \frac{1}{2\pi}\int_{\infty}^{-\infty} \zeta d\ln \frac{D(i\zeta)}{D_\infty(i\zeta)} \tag{F.37}$$

By performing integration by parts [74]:

$$\left(\sum_J \omega_J\right)_{ren} = \frac{1}{2\pi}\zeta \ln\frac{D(i\zeta)}{D_\infty(i\zeta)} - \frac{1}{2\pi}\int_{\infty}^{-\infty} d\zeta \ln\frac{D(i\zeta)}{D_\infty(i\zeta)} \tag{F.38}$$

$$= \frac{1}{2\pi}\int_{-\infty}^{\infty} d\zeta \ln\frac{D(i\zeta)}{D_\infty(i\zeta)} \tag{F.39}$$

Now, we substitute the normalized quantity obtained into the electromagnetic field's zero-point energy:

$$\frac{E^*}{L^2} = \frac{\hbar}{2}\int \frac{dk_\parallel}{(2\pi)^2}\sum_J \left(\omega_J^{(1)} + \omega_J^{(2)}\right) \tag{F.40}$$

$$= \frac{\hbar}{2\pi}\int_0^{+\infty} \frac{2\pi k dk}{(2\pi)^2}\int_{-\infty}^{\infty} d\zeta \ln\frac{D(i\zeta)}{D_\infty(i\zeta)} \tag{F.41}$$

Remember that $D(\omega_J)$ relates to both the frequency (ω_J) of parallel-polarized modes and

perpendicular-polarized ones. It is called [74] $Q_1(i\zeta) = \frac{D^{(1)}(i\zeta)}{D^{(1)}_\infty(i\zeta)}$ and $Q_2(i\zeta) = \frac{D^{(2)}(i\zeta)}{D^{(2)}_\infty(i\zeta)}$.

$$\frac{\hbar}{(2\pi)^2}\int_0^{+\infty} k dk \int_0^{\infty} d\zeta \left[\ln Q_1(i\zeta) + \ln Q_2(i\zeta)\right] \tag{F.42}$$

Introduce the variable $k^2 = \frac{\zeta}{c}(p^2 - 1)$:

$$\frac{\hbar}{(2\pi c)^2}\int_1^{+\infty} p dp \int_0^{\infty} \zeta^2 d\zeta \left[\ln Q_1(i\zeta) + \ln Q_2(i\zeta)\right] \tag{F.43}$$

The latter expresses a finite contribution to the Casimir energy density [75]. Let's now introduce the variable $k^2 = \frac{\zeta}{c}(p^2 - 1)$

$$\frac{\hbar}{(2\pi c)^2}\int_1^{+\infty} p\, dp \int_0^{\infty} \zeta^2\, d\zeta \left[\ln Q_1(i\zeta) + \ln Q_2(i\zeta)\right] \tag{F.44}$$

The Equation F.43 expresses a finite contribution to the Casimir energy density. We derive from it the Casimir force per unit area between the two half-spaces, introducing a new variable change $K = K(i\zeta) = \sqrt{p^2 - 1 + \varepsilon(i\zeta)} = \frac{c}{\zeta}R(i\zeta)$

$$\begin{aligned} F(d) &= -\frac{\partial E^*(d)}{\partial d} \\ &= -\frac{h}{2\pi^2 c^3}\int_1^{\infty} p^2\, dp \int_0^{\infty} \zeta^3\, d\zeta \left[\left(\left(\frac{K+\varepsilon p}{K-\varepsilon p}\right)^2 e^{-2\left(\frac{\zeta}{c}\right)pd} - 1\right)^{-1}\right. \\ &\quad \left. + \left(\left(\frac{K+p}{K-p}\right)^2 e^{-2\left(\frac{\zeta}{c}\right)pd} - 1\right)^{-1}\right] \end{aligned} \tag{F.45}$$

At distances comparable to the characteristic absorption length of dielectric materials ($d \ll \lambda_0$), the equations above can be written in a simpler form, which includes the Hamaker constant [76]:

$$I = \frac{3\hbar}{8\pi}\int_0^{\infty} x^2\, dx \int_0^{\infty} d\zeta \left[\left(\frac{\varepsilon+1}{\varepsilon-1}\right)^2 e^x - 1\right]^{-1} \tag{F.46}$$

where the integration variable used is $x = \frac{2vcd}{c}$, and the Casimir force and energy density become:

$$F = -\frac{H}{6\pi d^3}, \quad E^* = -\frac{H}{12\pi a^2} \tag{F.47}$$

the equation above:

$$E^* = -\frac{\hbar}{32\pi^2 d^2}\int_0^{\infty} d\omega \int_0^{\infty} dx\, x^2 \left[\left(\frac{\varepsilon(i\omega)+1}{\varepsilon(i\omega)-1}\right)^2 e^x - 1\right]^{-1} \tag{F.48}$$

which, in the limit of perfect conductors, reduces to the Casimir formula

$$E^*(d) = -\frac{\pi^2}{720}\frac{\hbar c}{a^3}. \tag{F.49}$$

Appendix G

Non-Specular Scattering

We will now present a more generalized formalism for calculating the Casimir force and energy, considering non-specular reflection by the plates. Non-specular reflection represents the general reflection process on any mirror, as opposed to specular reflection, which is an idealization.
We can rewrite the expression of the Casimir energy between two flat plates as a sum over modes labeled by ξ and $m \equiv \mathbf{k}, p$ [77]:

$$E_{\text{sp}} = \hbar \int_0^\infty \frac{\mathrm{d}\xi}{2\pi} \operatorname{Tr} \Delta_{\mathbf{k}}^p[i\xi], \quad \Delta_{\mathbf{k}}^p[i\xi] = \ln\left(1 - r_1 r_2 \mathrm{e}^{-2\kappa L}\right). \tag{G.1}$$

This can be interpreted as the energy stored inside the cavity during the scattering process. It is expressed in terms of the phase shifts $\Delta_{\mathbf{k}}^p[i\xi]$ acquired by the field modes upon scattering on the cavity. These phase shifts are deduced from the S-matrix of the cavity in such a manner that the Casimir energy is simply equal to the logarithm of the determinant of the S-matrix [1], this can also be written as the trace of a matrix, here diagonal, defined on these modes [29]:

$$E_{\text{sp}} = \hbar \int_0^\infty \frac{\mathrm{d}\xi}{2\pi} \sum_m \left\langle m \left| \ln\left(1 - r_1 r_2 \mathrm{e}^{-2\kappa_i L}\right) \right| m \right\rangle. \tag{G.2}$$

Here, r_1 and r_2 are diagonal matrices containing the specular reflection amplitudes as seen from fields inside the cavity:

$$\langle m \left| r_i \right| m' \rangle \equiv \delta_{m,m'} r_i(\xi, m), \quad \delta_{m,m'} \equiv 4\pi^2 \delta\left(\mathbf{k} - \mathbf{k}'\right) \delta_{p,p'}, \tag{G.3}$$

while κ is a diagonal matrix over the same modes:

$$\langle m | \kappa | m' \rangle \equiv \sqrt{\mathbf{k}_m^2 + \xi^2}\, \delta_{m,m'}. \tag{G.4}$$

[1] In physics, the S-matrix or scattering matrix relates the initial state and the final state of a physical system undergoing a scattering process

It is now straightforward to derive a more general formula for the Casimir energy in the case of stationary but non-specular scattering [29]:

$$E_{\text{nsp}} = \hbar \int_0^\infty \frac{\mathrm{d}\xi}{2\pi} \operatorname{Tr} \ln \left(1 - \mathcal{R}_1 \mathrm{e}^{-\kappa L} \mathcal{R}_2 \mathrm{e}^{-\kappa L}\right). \tag{G.5}$$

The two matrices $\mathcal{R}_1$ and $\mathcal{R}_2$ are no longer diagonal on plane waves since they describe non-specular reflection on the two mirrors. The propagation factors remain diagonal on plane waves [77].

Appendix H

Topological Insulators

H.1 Quantized Bulk Linear Magneto-Electric in Topological Insulators

The phenomenon of quantized (bulk) linear magneto-electric properties in topological insulators is a fascinating aspect of condensed matter physics. The material's constitutive equations are expressed in terms of electromagnetic parameters for regions (A) and (B) and the constitutive equations for the electromagnetic field in momentum space (D_k and H_k) are given by

$$\begin{aligned} D_k &= \varepsilon(\omega, k) \cdot E_k + v(\omega, k) \cdot B_k \\ H_k &= \zeta(\omega, k) \cdot E_k + \mu^{-1}(\omega, k) \cdot B_k \end{aligned} \tag{H.1}$$

These equations describe the intricate interplay of electric and magnetic properties in these unique materials, as reported in [34].

(a) (b)

Figure H.1: (A) Interface conditions between two media characterized by surface conductivities, denoted as σ_s^{A} and σ_s^{B} respectively. (B) Interface conditions between two media are characterized by surface conductivities indicated by the different θ values only.

Moreover, topological insulators, at finite frequencies, exhibit quantized bulk linear magneto-electric behaviour [78], where the quantities $\varepsilon^{A}(\omega)\mu^{A}(\omega)$ and $\varepsilon^{B}(\omega)\mu^{B}(\omega)$ play a crucial role. The introduction of the topological magnetoelectric polarizability (θ) further enriches the material's

characteristics. This polarizability is represented in a tabular form [33]: Furthermore, under time-reversal symmetry, the constitutive equation for H_k takes a simplified form

$$H_k = -\alpha\varepsilon_0 c\frac{\theta}{\pi}E_k + \mu^{-1}(\omega, k)\cdot B_k \tag{H.2}$$

In the absence of time-reversal symmetry, the topological magnetoelectric polarizability (θ) takes values in the set $\{..., -3\pi, -\pi, \pi, 3\pi, ...\}$. This intriguing behaviour highlights the rich physics underlying topological insulators. The constitutive equations, describing the relationship between electric and magnetic fields in momentum space, take the form

$$H_k = -\alpha\varepsilon_0 c\frac{\theta}{\pi}E_k + \mu^{-1}(\omega, k)\cdot B_k \tag{H.3}$$

This set of equations is crucial for understanding the intricate interplay between electric and magnetic responses in topological insulators [79].
Furthermore, the TMEP introduces polarization mixing, leading to non-zero coefficients r_{ps} and r_{sp} in the reflection coefficients. The relationships are given by:

$$(\mathbf{H}^{\mathrm{B}} - \mathbf{H}^{\wedge}) \times \hat{\mathbf{n}}^{\mathrm{AB}} = \mathbf{0}, \tag{H.4}$$

and

$$\mathbf{k} \times \mathbf{E}_{\mathbf{k}} - \omega\mathbf{B}_{\mathbf{k}} = \mathbf{0}. \tag{H.5}$$

It then follows that:

$$\begin{aligned} r_{ps} &\neq 0 \\ r_{sp} &\neq 0 \end{aligned} \tag{H.6}$$

These equations highlight the nontrivial impact of TMEP, indicating that the Casimir force in topological insulators involves a complex interplay of polarizations, paving the way for intriguing possibilities in nanoscale physics and quantum technologies.

H.2 Topological Insulators vs Topologically Trivial Materials

The distinction between topological insulators and topologically trivial materials can be captured by the parameter θ, which classifies time-reversal ($\mathcal{T}$) invariant insulators. The value of θ determines the topological nature of the material [80]:

- For $\theta = 0 \bmod (2\pi) \Rightarrow me^{i\theta\gamma_5} = m > 0$, the material is topologically trivial.
- For $\theta = \pi(2n+1) \Rightarrow me^{i\theta\gamma_5} = -m < 0$, the material is a topological insulator.

(a) (b)

Figure H.2: Comparison between topologically trivial material (A) and topological insulator (B).

H.2.1 Axion Electrodynamics

The EM response of a topological insulator can be described by the following Lagrangian [81]:

$$\mathcal{L} = \frac{1}{2}\left(\epsilon \mathbf{E}^2 + \mu^{-1}\mathbf{B}^2\right) + \frac{\alpha\theta}{2\pi}\mathbf{E}\cdot\mathbf{B} + \mathcal{F}^{\mu}A_{\mu}. \tag{H.7}$$

This leads to a set of modified Maxwell's equations, often referred to as axion electrodynamics [60]:

$$\begin{aligned}
\vec{\nabla}\cdot\mathbf{E} &= \rho - \frac{\alpha}{\pi}\mathbf{B}\cdot\vec{\nabla}\theta, \\
\vec{\nabla}\times\mathbf{E} &= -\partial_t\mathbf{B}, \\
\vec{\nabla}\cdot\mathbf{B} &= 0, \\
\vec{\nabla}\times\mathbf{B} &= \mathbf{J} + \partial_t\mathbf{E} + \frac{\alpha}{\pi}\dot{\theta}\mathbf{B} - \frac{\alpha}{\pi}\mathbf{E}\times\vec{\nabla}\theta.
\end{aligned} \tag{H.8}$$

If θ is constant, electrodynamics remain unchanged, but if $\dot{\theta} \neq 0$, magnetoelectric couplings arise, leading to modified constitutive relations [82]:

$$\mathbf{D} = \epsilon\mathbf{E} + \frac{\alpha\theta}{\pi}\mathbf{B}, \tag{H.9}$$

$$\mathbf{H} = \mu^{-1}\mathbf{B} - \frac{\alpha\theta}{\pi}\mathbf{E}. \tag{H.10}$$

H.2.2 Surface of a Topological Insulator

Inside the bulk of a topological insulator, the action is described by [83]:

$$S_{TI} = \int d^3x\, dt\, \left(\frac{1}{2}\left(\epsilon\mathbf{E}^2 + \mu^{-1}\mathbf{B}^2\right) + \frac{\alpha\theta}{2\pi}\mathbf{E}\cdot\mathbf{B}\right) = S_{\text{die}} + S_{\theta}. \tag{H.11}$$

At the boundary, Stokes' theorem gives the surface contribution to the action [68]:

$$S_{\theta} = \theta\frac{\alpha}{4\pi}\int d^2x\, dt\, \epsilon^{\nu\rho\sigma}\left(A_{\nu}\partial_{\rho}A_{\sigma}\right). \tag{H.12}$$

This is analogous to the action for the Quantum Hall Effect (QHE) [69]:

$$S_{QHE} = \frac{\sigma_{xy}}{2} \int d^2x\, dt\, \epsilon^{\nu\rho\sigma} \left(A_\nu \partial_\rho A_\sigma \right), \tag{H.13}$$

where $\theta = (2n+1)\pi \Rightarrow \sigma_{xy} = \theta \frac{\alpha}{2\pi} = \frac{e^2}{h}\left(n + \frac{1}{2}\right)$. This equation encapsulates the connection between the topological properties of a material and its observable physical phenomena, specifically the quantum Hall effect (QHE). The action S_{QHE} describes the quantized Hall conductivity σ_{xy}, which arises due to the presence of a non-trivial θ term. When θ is quantized to $(2n+1)\pi$, the Hall conductivity σ_{xy} is given by $\frac{e^2}{h}(n + \frac{1}{2})$, indicating half-integer quantization [83]. This result is a hallmark of the topological insulator's edge states, which conduct electricity in a manner robust against local perturbations [80]. Thus, the equation highlights the profound impact of topological order on electronic transport properties, bridging abstract theoretical concepts with measurable experimental effects in condensed matter physics.

Appendix I

Additional Results Analysis Liquids

I.0.1 T-test Results

We performed pairwise t-tests to compare the means of the TFC data between each pair of liquids corresponding to the same values of θs, to assess whether the means of two groups are statistically different, as differences in TFC could reflect variations in physical properties such as viscosity, density, or molecular interactions in the real of Casimir Force measurements [84].
For each comparison:

- Calculate the t-statistic: A value that measures the size of the difference relative to the variation in your sample data [84].
- Determine the p-value: A probability that measures the evidence against the null hypothesis (which states there is no difference in the means) [84].

The results of the t-tests are summarized below:
Glycerol vs. Water:
The t-test comparing the TFC data between glycerol and water yielded a t-statistic of 1.816 ($df = 7198$ [1], $p = 0.0694$). The obtained p-value suggests that there is not enough evidence to reject the null hypothesis, indicating that the means of the TFC data for glycerol and water are not significantly different at the 0.05 significance level.
Glycerol vs. Methanol:
In contrast, the t-test comparing the TFC data between glycerol and methanol revealed a statistically significant difference ($t = 2.562$, $df = 8398$ [1], $p = 0.0104$). The obtained p-value indicates that the means of the TFC data for glycerol and methanol are significantly different at the 0.05 significance level.
Water vs. Methanol:
Similarly, the t-test comparing the TFC data between water and methanol showed no significant

[1] df indicates the degrees of freedom, which reflect the number of independent values in a data set that can vary, in this case the number of distances values included.

difference ($t = 0.730$, $df = 7198$ [1], $p = 0.4654$), suggesting that the means of the TFC data for water and methanol are not significantly different at the 0.05 significance level.

I.0.2 ANOVA Results

Unlike t-tests that compare two groups at a time, Analysis of Variance (ANOVA) can handle multiple groups simultaneously. We compared the means of the TFC data among all three liquids.
ANOVA calculates an F-statistic, which is a ratio of the variance between the group means to the variance within the groups. A corresponding p-value determines the significance of the result [84]. If the p-value is less than the chosen significance level (usually 0.05), it suggests that at least one group mean is significantly different from the others.
The ANOVA test in the first 10 nm yielded a statistically significant result ($F = 4.050$, $p = 0.0174$), indicating that there are no significant differences in the means of the TFC data among glycerol, water, and methanol.

Appendix J

Additional Results TI Multilayers

J.1 Statistical analysis of section 4.3

J.1.1 T-Test Results

For both $\theta = 5$ and $\theta = -5$, the analysis of topological force contrast (TFC) across different thicknesses yielded interesting insights.

For $\theta = 5$:

- TFC Comparison for Thicknesses 0.4nm and 14nm: A significant difference was found in TFC values between these thicknesses (T-Statistic: -4.8589, P-Value: 1.51e-06), indicating an influence of thickness on TFC for $\theta = 5$. However, no significant differences were observed in TFC values between other thickness pairs (0.4nm vs. 4nm, 0.4nm vs. 40nm, 4nm vs. 14nm, 4nm vs. 40nm, 14nm vs. 40nm).

For $\theta = -5$:

- TFC Comparison for Thicknesses 0.4nm and 14nm: Similarly, a significant difference was found in TFC values between these thicknesses (T-Statistic: -22.7603, P-Value: 3.87e-83), highlighting the impact of thickness on TFC for $\theta = -5$. As with $\theta = 5$, no significant differences were observed in TFC values between other thickness pairs (0.4nm vs. 4nm, 0.4nm vs. 40nm, 4nm vs. 14nm, 4nm vs. 40nm, 14nm vs. 40nm).

These findings suggest that, for both θ orientations, variations in thickness notably influence TFC only between specific thickness pairs. This underscores the importance of considering the interplay between thickness and TFC in the analysis and interpretation of experimental results.

Bibliography

[1] H. B. G. Casimir, "On the attraction between two perfectly conducting plates," *Indag. Math.*, vol. 10, no. 4, pp. 261–263, 1948.

[2] E. M. Lifshitz, M Hamermesh, *et al.*, "The theory of molecular attractive forces between solids," in *Perspectives in theoretical physics*, Elsevier, 1992, pp. 329–349.

[3] T. Emig, A. Hanke, R. Golestanian, and M. Kardar, "Probing the strong boundary shape dependence of the casimir force," *Phys. Rev. Lett.*, vol. 87, p. 260 402, 2001. doi: 10.1103/PhysRevLett.87.260402. arXiv: cond-mat/0106028.

[4] H. B. G. Casimir and D. Polder, "The Influence of retardation on the London-van der Waals forces," *Phys. Rev.*, vol. 73, pp. 360–372, 1948. doi: 10.1103/PhysRev.73.360.

[5] B. Spreng, M. Hartmann, V. Henning, P. A. M. Neto, and G.-L. Ingold, "Proximity force approximation and specular reflection: Application of the wkb limit of mie scattering to the casimir effect," *Physical Review A*, vol. 97, no. 6, p. 062 504, 2018.

[6] S. A. Ellingsen, I. Brevik, J. S. Høye, and K. A. Milton, "Temperature correction to casimir-lifshitz free energy at low temperatures: Semiconductors," *Phys. Rev. E*, vol. 78, p. 021 117, 2 2008. doi: 10.1103/PhysRevE.78.021117. [Online]. Available: https://link.aps.org/doi/10.1103/PhysRevE.78.021117.

[7] C. G. Someda, *Electromagnetic waves*. Crc Press, 2017.

[8] V. Nesterenko and I. Pirozhenko, "Simple method for calculating the casimir energy for a sphere," *Physical Review D*, vol. 57, no. 2, p. 1284, 1998.

[9] M. J. Sparnaay, "Measurements of attractive forces between flat plates," *Physica*, vol. 24, no. 6-10, pp. 751–764, 1958.

[10] E. M. Lifshitz, "The theory of molecular attractive forces between solids," *Sov. Phys. JETP*, vol. 2, pp. 73–83, 1956.

[11] J.-J. Greffet, "Introduction to surface plasmon theory," in *Plasmonics: From Basics to Advanced Topics*, Springer, 2012, pp. 105–148.

[12] J. S. Høye, "Van der waals interactions: Evaluations by use of a statistical mechanical method," *The Journal of chemical physics*, vol. 135, no. 13, 2011.

[13] D Drosdoff and L. M. Woods, "Casimir forces and graphene sheets," *Physical Review B*, vol. 82, no. 15, p. 155 459, 2010.

[14] A. Rodriguez, M. Ibanescu, D. Iannuzzi, F. Capasso, J. D. Joannopoulos, and S. G. Johnson, "Computation and visualization of casimir forces in arbitrary geometries: Nonmonotonic lateral-wall forces and the failure of proximity-force approximations," *Phys. Rev. Lett.*, vol. 99, p. 080 401, 8 2007. doi: 10.1103/PhysRevLett.99.080401. [Online]. Available: https://link.aps.org/doi/10.1103/PhysRevLett.99.080401.

[15] G. Palasantzas, M. Sedighi, and V. B. Svetovoy, "Applications of Casimir forces: Nanoscale actuation and adhesion," *Applied Physics Letters*, vol. 117, no. 12, p. 120 501, Sep. 2020, issn: 0003-6951. doi: 10.1063/5.0023150. eprint: https://pubs.aip.org/aip/apl/article-pdf/doi/10.1063/5.0023150/19780953/120501_1_online.pdf. [Online]. Available: https://doi.org/10.1063/5.0023150.

[16] Y Bao, R Guerout, J Lussange, *et al.*, "Casimir force on a surface with shallow nanoscale corrugations: Geometry and finite conductivity effects," *Physical Review Letters*, vol. 105, no. 25, Dec. 2010, issn: 0031-9007. doi: 10.1103/PHYSREVLETT.105.250402. [Online]. Available: https://www.osti.gov/biblio/21554471.

[17] R. S. Decca, E Fischbach, G. L. Klimchitskaya, *et al.*, "Application of the proximity force approximation to gravitational and yukawa-type forces," *Physical Review. D, Particles Fields*, vol. 79, no. 12, Jun. 2009, issn: 0556-2821. doi: 10.1103/PHYSREVD.79.124021. [Online]. Available: https://www.osti.gov/biblio/21300980.

[18] Z. Lenac and M.-S. Tomaš, "Casimir force on a thin slab: The influence of surrounding media and the role of surface polaritons," *Physical Review A*, vol. 78, no. 2, p. 023 834, 2008.

[19] R Zhao, T. Koschny, E. Economou, and C. Soukoulis, "Repulsive casimir forces with finite-thickness slabs," *Physical Review B*, vol. 83, no. 7, p. 075 108, 2011.

[20] J. E. Moore, "The birth of topological insulators," *Nature*, vol. 464, no. 7286, pp. 194–198, 2010.

[21] L. Fu, C. L. Kane, and E. J. Mele, "Topological insulators in three dimensions," *Physical review letters*, vol. 98, no. 10, p. 106 803, 2007.

[22] X.-L. Qi and S.-C. Zhang, "The quantum spin hall effect and topological insulators," *Physics Today*, vol. 63, Jan. 2010. doi: 10.1063/1.3293411.

[23] R. D. Peccei and H. R. Quinn, "CP Conservation in the presence of pseudoparticles," *Phys. Rev. Lett.*, vol. 38, pp. 1440–1443, 25 1977. doi: 10.1103/PhysRevLett.38.1440. [Online]. Available: https://link.aps.org/doi/10.1103/PhysRevLett.38.1440.

[24] A. G. Grushin, P. Rodriguez-Lopez, and A. Cortijo, "Effect of finite temperature and uniaxial anisotropy on the casimir effect with three-dimensional topological insulators," *Physical Review B*, vol. 84, no. 4, p. 045 119, 2011.

[25] M. Krech, "Casimir forces in binary liquid mixtures," *Physical Review E*, vol. 56, no. 2, p. 1642, 1997.

[26] M. Parkhomenko, D. Kalenov, N. A. Fedoseev, I. Eremin, V. M. Kolesnikova, and D. A. Kovtykov, "The improved resonator method for measuring the complex permittivity of materials," *Journal of Communications Technology and Electronics*, vol. 62, pp. 759–764, 2017. doi: 10.1134/S106422691706016X.

[27] K.-L. Zhang, Z. Hou, L. Kong, H. Fang, and K.-T. Zhan, "Origin of negative imaginary part of effective permittivity of passive materials," *Chinese Physics Letters*, vol. 34, no. 9, 2017. doi: 10.1088/0256-307X/34/9/097701. [Online]. Available: https://iopscience.iop.org/article/10.1088/0256-307X/34/9/097701.

[28] G. Klimchitskaya and V. Mostepanenko, "Casimir free energy of metallic films: Discriminating between drude and plasma model approaches," *Physical Review A*, vol. 92, no. 4, p. 042 109, 2015.

[29] A. Lambrecht, P. A. M. Neto, and S. Reynaud, "The casimir effect within scattering theory," *New Journal of physics*, vol. 8, no. 10, p. 243, 2006.

[30] R. L. Jaffe, "Casimir effect and the quantum vacuum," *Physical review D*, vol. 72, no. 2, p. 021 301, 2005.

[31] Z. H. Liu and S. A. Fulling, "Casimir energy with a robin boundary: The multiple-reflection cylinder-kernel expansion," *New Journal of Physics*, vol. 8, no. 10, p. 234, 2006. doi: 10.1088/1367-2630/8/10/234. [Online]. Available: https://dx.doi.org/10.1088/1367-2630/8/10/234.

[32] I. Pirozhenko and A. Lambrecht, "Influence of slab thickness on the casimir force," *Phys. Rev. A*, vol. 77, p. 013 811, 1 2008. doi: 10.1103/PhysRevA.77.013811. [Online]. Available: https://link.aps.org/doi/10.1103/PhysRevA.77.013811.

[33] G. Chavez Ponce de Leon, *Casimir forces between topological insulators*, Student Thesis, 2023. [Online]. Available: https://fse.studenttheses.ub.rug.nl/30172/.

[34] X.-L. Qi, T. L. Hughes, and S.-C. Zhang, "Topological field theory of time-reversal invariant insulators," *Phys. Rev. B*, vol. 78, p. 195 424, 19 2008. doi: 10.1103/PhysRevB.78.195424. [Online]. Available: https://link.aps.org/doi/10.1103/PhysRevB.78.195424.

[35] J. C. Martinez and M. B. A. Jalil, "Tuning the Casimir force via modification of interface properties of three-dimensional topological insulators," *Journal of Applied Physics*, vol. 113, no. 20, p. 204 302, May 2013, issn: 0021-8979. doi: 10.1063/1.4807796. eprint: https://pubs.aip.org/aip/jap/article-pdf/doi/10.1063/1.4807796/9106561/204302_1_online.pdf. [Online]. Available: https://doi.org/10.1063/1.4807796.

[36] J. Wang, C. Gorini, K. Richter, Z. Wang, Y. Ando, and D. Weiss, *Probing the coulomb gap in the topological insulator bisbtese$_2$ via quantum capacitance*, Dec. 2019.

[37] W. Nie, R. Zeng, Y. Lan, and S. Zhu, "Casimir force between topological insulator slabs," *Phys. Rev. B*, vol. 88, p. 085 421, 8 2013. doi: 10.1103/PhysRevB.88.085421. [Online]. Available: https://link.aps.org/doi/10.1103/PhysRevB.88.085421.

[38] G. Klimchitskaya, U Mohideen, and V. Mostepanenko, "The casimir force between real materials: Experiment and theory," *Reviews of Modern Physics*, vol. 81, no. 4, p. 1827, 2009.

[39] G. Palasantzas, V. Svetovoy, and P. Van Zwol, "Influence of ultrathin water layer on the van der waals/casimir force between gold surfaces," *Physical Review B*, vol. 79, no. 23, p. 235 434, 2009.

[40] B. Ninham and V. Parsegian, "Van der waals forces: Special characteristics in lipid-water systems and a general method of calculation based on the lifshitz theory," *Biophysical journal*, vol. 10, no. 7, pp. 646–663, 1970.

[41] A. Gambassi, A. Maciołek, C. Hertlein, *et al.*, "Critical casimir effect in classical binary liquid mixtures," *Physical Review E*, vol. 80, no. 6, p. 061 143, 2009.

[42] C. J. V. Oss, M. K. Chaudhury, and R. J. Good, "Interfacial lifshitz-van der waals and polar interactions in macroscopic systems," *Chemical Reviews*, vol. 88, no. 6, pp. 927–941, 1988. doi: 10.1021/cr00088a006.

[43] Z. Lenac, "Casimir force on a thin slab: The influence of surrounding media and the role of surface polaritons," *Phys. Rev. A*, vol. 78, p. 023 834, 2 2008. doi: 10.1103/PhysRevA.78.023834. [Online]. Available: https://link.aps.org/doi/10.1103/PhysRevA.78.023834.

[44] R. Passante, L. Rizzuto, S. Spagnolo, S. Tanaka, and T. Y. Petrosky, "Harmonic oscillator model for the atom-surface casimir-polder interaction energy," *Physical Review A*, vol. 85, no. 6, p. 062 109, 2 2012. doi: 10.1103/PhysRevA.78.023834. [Online]. Available: https://link.aps.org/doi/10.1103/PhysRevA.78.023834.

[45] V. Dodonov and A. Dodonov, "Quantum harmonic oscillator and nonstationary casimir effect," *Journal of Russian Laser Research*, vol. 26, pp. 445–483, 2 2005. doi: 10.1103/PhysRevA.78.023834. [Online]. Available: https://link.aps.org/doi/10.1103/PhysRevA.78.023834.

[46] L. Teuber and S. Scheel, "Solving the quantum master equation of coupled harmonic oscillators with lie-algebra methods," *Physical Review A*, vol. 101, no. 4, p. 042 124, 2 2020. doi: 10.1103/PhysRevA.78.023834. [Online]. Available: https://link.aps.org/doi/10.1103/PhysRevA.78.023834.

[47] M Rushka and J. Freericks, "A completely algebraic solution of the simple harmonic oscillator," *American Journal of Physics*, vol. 88, no. 11, pp. 976–985, 2 2020. doi: 10.1103/PhysRevA.78.023834. [Online]. Available: https://link.aps.org/doi/10.1103/PhysRevA.78.023834.

[48] M Arik and D. D. Coon, "Hilbert spaces of analytic functions and generalized coherent states," *Journal of Mathematical Physics*, vol. 17, no. 4, pp. 524–527, 2 1976. doi: 10.1103/PhysRevA.78.023834. [Online]. Available: https://link.aps.org/doi/10.1103/PhysRevA.78.023834.

[49] K. A. Milton, "Local and global casimir energies: Divergences, renormalization, and the coupling to gravity," in *Casimir Physics*, D. Dalvit, P. Milonni, D. Roberts, and F. da Rosa, Eds. Berlin, Heidelberg: Springer Berlin Heidelberg, 2011, vol. 78, pp. 39–95, isbn: 978-3-642-20288-9. doi: 10.1007/978-3-642-20288-9_3. [Online]. Available: https://doi.org/10.1007/978-3-642-20288-9_3.

[50] A. A. Saharian, R. S. Davtyan, and A. H. Yeranyan, "Casimir energy in the fulling-rindler vacuum," *Phys. Rev. D*, vol. 69, p. 085 002, 8 2004. doi: 10.1103/PhysRevD.69.085002. [Online]. Available: https://link.aps.org/doi/10.1103/PhysRevD.69.085002.

[51] R. Courant, F. John, A. A. Blank, and A. Solomon, *Introduction to calculus and analysis*. Springer, 1965, vol. 1, p. 023 834. doi: 10.1103/PhysRevA.78.023834. [Online]. Available: https://link.aps.org/doi/10.1103/PhysRevA.78.023834.

[52] K. V. Shajesh, I. Brevik, I. Cavero-Peláez, and P. Parashar, "Self-similar plates: Casimir energies," *arXiv: High Energy Physics - Theory*, vol. 78, p. 023 834, 2 2016. doi: 10.1103/PhysRevA.78.023834. [Online]. Available: https://link.aps.org/doi/10.1103/PhysRevA.78.023834.

[53] A. Lambrecht and S. Reynaud, "Casimir force between metallic mirrors," *The European Physical Journal D*, vol. 8, pp. 309–318, 2 2000. doi: 10.1103/PhysRevA.78.023834. [Online]. Available: https://link.aps.org/doi/10.1103/PhysRevA.78.023834.

[54] A. Sushkov, W. Kim, D. Dalvit, and S. Lamoreaux, "Observation of the thermal casimir force," *Nature Physics*, vol. 7, no. 3, pp. 230–233, 2 2011. doi: 10.1103/PhysRevA.78.023834. [Online]. Available: https://link.aps.org/doi/10.1103/PhysRevA.78.023834.

[55] B. Harris, F Chen, and U Mohideen, "Precision measurement of the casimir force using gold surfaces," *Physical Review A*, vol. 62, no. 5, p. 052 109, 2 2000. doi: 10.1103/PhysRevA.78.023834. [Online]. Available: https://link.aps.org/doi/10.1103/PhysRevA.78.023834.

[56] G. Klimchitskaya and V. Mostepanenko, "Experiment and theory in the casimir effect," *Contemporary Physics*, vol. 47, no. 3, pp. 131–144, 2 2006. doi: 10.1103/PhysRevA.78.023834. [Online]. Available: https://link.aps.org/doi/10.1103/PhysRevA.78.023834.

[57] P. H. van Blokland and J. T. G. Overbeek, "Van der waals forces between objects covered with a chromium layer," *Journal of the Chemical Society, Faraday Transactions 1: Physical Chemistry in Condensed Phases*, vol. 74, pp. 2637–2651, 2 1978. doi: 10.1103/PhysRevA.78.023834. [Online]. Available: https://link.aps.org/doi/10.1103/PhysRevA.78.023834.

[58] S. K. Lamoreaux, "The casimir force: Background, experiments, and applications," *Reports on progress in Physics*, vol. 68, no. 1, p. 201, 2 2004. doi: 10.1103/PhysRevA.78.023834. [Online]. Available: https://link.aps.org/doi/10.1103/PhysRevA.78.023834.

[59] P. Bongaarts, "Maxwell's equations in axiomatic quantum field theory. i. field tensor and potentials," *Journal of Mathematical Physics*, vol. 18, pp. 1510–1516, 2 1977. doi: 10.1063/1.523414. [Online]. Available: https://link.aps.org/doi/10.1103/PhysRevA.78.023834.

[60] P. G. Huray, *Maxwell's equations*. John Wiley & Sons, 2009, vol. 78, p. 023 834. doi: 10.1103/PhysRevA.78.023834. [Online]. Available: https://link.aps.org/doi/10.1103/PhysRevA.78.023834.

[61] D. J. Griffiths, *Introduction to electrodynamics*. Cambridge University Press, 2023, vol. 78, p. 023 834. doi: 10.1103/PhysRevA.78.023834. [Online]. Available: https://link.aps.org/doi/10.1103/PhysRevA.78.023834.

[62] X. Wang, F. Wang, Lanzhigao, and R. Chen, "Understanding and application of gauss theorem in electrostatic field," in *2011 International Conference on Intelligence Science and Information Engineering*, vol. 78, American Physical Society, 2011, pp. 386–388. doi: 10.1109/ISIE.2011.118. [Online]. Available: https://link.aps.org/doi/10.1103/PhysRevA.78.023834.

[63] R. Good, "Particle aspect of the electromagnetic field equations," *Physical Review*, vol. 105, pp. 1914–1919, 2 1957. doi: 10.1103/PHYSREV.105.1914. [Online]. Available: https://link.aps.org/doi/10.1103/PhysRevA.78.023834.

[64] T. Fujita and N. Kanda, "Fundamental problems in quantum field theory," in *Quantum Field Theory*. American Physical Society, 2013, vol. 78, p. 023 834. doi: 10.2174/97816080575591130101. [Online]. Available: https://link.aps.org/doi/10.1103/PhysRevA.78.023834.

[65] D. J. Griffiths, *Introduction to Electrodynamics*, 4th ed. Cambridge University Press, 2017, vol. 78, p. 023 834. doi: 10.1103/PhysRevA.78.023834. [Online]. Available: https://link.aps.org/doi/10.1103/PhysRevA.78.023834.

[66] M. Fahmy, "The derivation of maxwell's equations from the equations of the quantum theory," *Proceedings of the Physical Society*, vol. 44, pp. 368–373, 2 1932. doi: 10.1088/0959-5309/44/3/313. [Online]. Available: https://link.aps.org/doi/10.1103/PhysRevA.78.023834.

[67] Y. Aharonov and D. Bohm, "Significance of electromagnetic potentials in the quantum theory," *Physical review*, vol. 115, no. 3, p. 485, 2 1959. doi: 10.1103/PhysRevA.78.023834. [Online]. Available: https://link.aps.org/doi/10.1103/PhysRevA.78.023834.

[68] Y. D. Chong, "Quantum field theory in a nutshell," *Phys. Rev. A*, vol. 78, p. 023 834, 2 2018. doi: 10.5860/choice.48-1536. [Online]. Available: https://link.aps.org/doi/10.1103/PhysRevA.78.023834.

[69] A. Michaud, "Electromagnetism according to maxwell's initial interpretation," *Journal of Modern Physics*, vol. 78, p. 023 834, 2 2020. doi: 10.4236/jmp.2020.111003. [Online]. Available: https://link.aps.org/doi/10.1103/PhysRevA.78.023834.

[70] A. Gersten, "Maxwell equations—the one-photon quantum equation," *Foundations of Physics*, vol. 31, pp. 1211–1231, 2 1999. doi: 10.1023/A:1017551920941. [Online]. Available: https://link.aps.org/doi/10.1103/PhysRevA.78.023834.

[71] C. C. Ttira, C. Fosco, and F. Mazzitelli, "Lifshitz formula for the casimir force and the gelfand–yaglom theorem," *Journal of Physics A: Mathematical and Theoretical*, vol. 44, p. 465 403, 2 2011. doi: 10.1088/1751-8113/44/46/465403. [Online]. Available: https://link.aps.org/doi/10.1103/PhysRevA.78.023834.

[72] M. Miralaei and R. Moazzemi, "Lifshitz formula using box renormalization (in persian)," *arXiv: Quantum Physics*, vol. 78, p. 023 834, 2 2018. doi: 10.1103/PhysRevA.78.023834. [Online]. Available: https://link.aps.org/doi/10.1103/PhysRevA.78.023834.

[73] S. Ellingsen, I. Brevik, J. Høye, and K. Milton, "Temperature correction to casimir-lifshitz free energy at low temperatures: Semiconductors," *Physical review. E, Statistical, nonlinear, and soft matter physics*, vol. 78(2 Pt 1), p. 021 117, 2 2008. doi: 10.1103/PhysRevE.78.021117. [Online]. Available: https://link.aps.org/doi/10.1103/PhysRevA.78.023834.

[74] T. Philbin, "Casimir effect from macroscopic quantum electrodynamics," *New Journal of Physics*, vol. 13, p. 063 026, 2 2011. doi: 10.1088/1367-2630/13/6/063026. [Online]. Available: https://link.aps.org/doi/10.1103/PhysRevA.78.023834.

[75] K. Milton, "Recent developments in the casimir effect," *arXiv: High Energy Physics - Theory*, vol. 161, p. 012 001, 2 2008. doi: 10.1088/1742-6596/161/1/012001. [Online]. Available: https://link.aps.org/doi/10.1103/PhysRevA.78.023834.

[76] D. Kobe, "Derivation of maxwell's equations from the local gauge invariance of quantum mechanics," *American Journal of Physics*, vol. 46, pp. 342–348, 2 1978. doi: 10.1119/1.11327. [Online]. Available: https://link.aps.org/doi/10.1103/PhysRevA.78.023834.

[77] J Penfold and R. Thomas, "The application of the specular reflection of neutrons to the study of surfaces and interfaces," *Journal of Physics: Condensed Matter*, vol. 2, no. 6, p. 1369, 2 1990. doi: 10.1103/PhysRevA.78.023834. [Online]. Available: https://link.aps.org/doi/10.1103/PhysRevA.78.023834.

[78] N. Armitage and L. Wu, "On the matter of topological insulators as magnetoelectrics," *SciPost Physics*, vol. 6, p. 023 834, 2 Apr. 2019. doi: 10.21468/SciPostPhys.6.4.046. [Online]. Available: https://link.aps.org/doi/10.1103/PhysRevA.78.023834.

[79] M. Zahradník, "Dynamic control of magnetization for spintronic applications studied by magneto-optical methods," Ph.D. dissertation, Université Paris-Saclay (ComUE), 2019, p. 023 834. doi: 10.1103/PhysRevA.78.023834. [Online]. Available: https://link.aps.org/doi/10.1103/PhysRevA.78.023834.

[80] S.-Q. Shen, *Topological Insulators: Dirac Equation in Condensed Matter*. Springer, 2012, vol. 78, p. 023 834, isbn: 978-3-642-32857-2. doi: 10.1103/PhysRevA.78.023834. [Online]. Available: https://link.aps.org/doi/10.1103/PhysRevA.78.023834.

[81] B. A. Bernevig and T. L. Hughes, *Topological Insulators and Topological Superconductors*. Princeton University Press, 2013, vol. 78, p. 023 834, isbn: 978-0-691-15175-5. doi: 10.1103/PhysRevA.78.023834. [Online]. Available: https://link.aps.org/doi/10.1103/PhysRevA.78.023834.

[82] V. Bezerra, G. L. Klimchitskaya, and V. Mostepanenko, "Correlation of energy and free energy for the thermal casimir force between real metals," *Physical Review A*, vol. 66, p. 062 112, 2 2002. doi: 10.1103/PhysRevA.66.062112. [Online]. Available: https://link.aps.org/doi/10.1103/PhysRevA.78.023834.

[83] Z. Lenac, *Topological Insulators* (Contemporary Concepts of Condensed Matter Science), M. Franz and L. Molenkamp, Eds. Elsevier, 2013, vol. 6, p. 023 834, isbn: 978-0-444-63314-9. doi: 10.1103/PhysRevA.78.023834. [Online]. Available: https://link.aps.org/doi/10.1103/PhysRevA.78.023834.

[84] H. M. Park, “Comparing group means: T-tests and one-way anova using stata, sas, r, and spss,” *Phys. Rev. A*, Contemporary Concepts of Condensed Matter Science, vol. 6, M. Franz and L. Molenkamp, Eds., p. 023 834, 2 2009. doi: 10.1103/PhysRevA.78.023834. [Online]. Available: https://link.aps.org/doi/10.1103/PhysRevA.78.023834.